An embedded disk (eDisk) in the IceAge: investigating the jet and outflow from Ced 110 IRS4

Narang, M.; Ohashi, N.; Tobin, J.J.; McClure, M.K.; Jørgensen, J.K.; Sai (Insa Choi), J.

The Astronomical Journal, 169:192 (17pp), 2025 April https://doi.org/10.3847/1538-3881/adb1ba

An Embedded Disk (eDisk) in the IceAge: Investigating the Jet and Outflow from Ced 110 IRS4

Mayank Narang[1], Nagayoshi Ohashi[1], John J. Tobin[2], M. K. McClure[3], Jes K. Jørgensen[4], and Jinshi Sai (Insa Choi)[1]
eDisk + IceAge Team

[1] Academia Sinica Institute of Astronomy and Astrophysics, 11F of Astronomy-Mathematics Building, AS/NTU, No. 1, Sec. 4, Roosevelt Rd., Taipei 106216, Taiwan
[2] National Radio Astronomy Observatory, 520 Edgemont Rd., Charlottesville, VA 22903, USA
[3] Leiden Observatory, Leiden University, PO Box 9513, NL-2300 RA Leiden, The Netherlands
[4] Niels Bohr Institute, University of Copenhagen, Øster Voldgade 5-7, 1350, Copenhagen, Denmark
Received 2024 November 6; revised 2025 January 30; accepted 2025 January 31; published 2025 March 4

Abstract

We present a comprehensive study of the large-scale structure, jet and outflow morphology, and kinematics of the Class 0/I protostellar binary Ced 110 IRS4, using JWST NIRCam (F150W and F410M) and MIRI MRS observations from the JWST ERC program IceAge, along with Atacama Large Millimeter/submillimeter Array (ALMA) data from the Early Planet Formation in Embedded Disks (eDisk) program. NIRCam images, combined with ALMA continuum and CO data, reveal arc-like structures (∼1100 au), suggesting a dense envelope around the protostars. We detect disk shadows from both protostars in F150W. The MIRI MRS integral field unit data reveal a jet from both protostars in multiple [Fe II] lines, [Ar II] 6.99 μm and [Ne II] 12.81 μm, marking the first detection of a jet from the system. The [Fe II] (5.34 μm) jet from Ced 110 IRS4A has a width of $\leqslant$51 au at the protostellar location, with a large opening angle of 23° ± 4°. After inclination correction, the jet velocity is 124 km s^{-1}, corresponding to a dynamical timescale of 25 yr. The molecular H_2 outflow displays a distinct morphology resembling two hemispheres placed back-to-back. The consistent H_2 emission extent across transitions, differing from previous observations of protostellar outflows detected with JWST, suggests that MHD disk winds may not drive the observed outflow. We find that the upper limit to the width of the outflow at the protostellar location is 130 ± 10 au, which is smaller than the disk diameter of 183.4 ± 0.4 au but much larger than width of the [Fe II] jet.

Unified Astronomy Thesaurus concepts: Protostars (1302); Young stellar objects (1834); Stellar jets (1607); Stellar winds (1636)

1. Introduction

Class 0 protostars represent the earliest phase of star formation and are empirically defined as having bolometric temperature $T_{bol} < 70$ K or $L_{smm}/L_{bol} > 0.005$ (e.g., P. Andre et al. 1993; R. J. White et al. 2007; N. J. Evans et al. 2009; M. M. Dunham et al. 2014; J. J. Tobin & P. D. Sheehan 2024). Class 0 protostars possess dense circumstellar envelopes that feed the protostellar disk (R. K. Ulrich 1976; P. Cassen & A. Moosman 1981), which in turn accretes onto the central star. These protostars also drive strong bipolar jets/outflows (R. E. Pudritz et al. 2007; H. Shang et al. 2007; A. Frank et al. 2014; J. Bally 2016; L. Hartmann et al. 2016; T. P. Ray & J. Ferreira 2021), which remove angular momentum from protostellar disks and thus maintain the accretion.

The low mass accretion rates measured from more evolved protostars Class I and flat-spectrum sourcesusing optical and near-IR (NIR) spectra suggest that most of the accretion occurs in the earlier Class 0 phase (R. J. White & L. A. Hillenbrand 2004; E. Fiorellino et al. 2022, 2023; M. Narang et al. 2023). However, protostars in their primary accretion phase are deeply embedded within dense envelopes, making it difficult for direct detection of accretion tracers in the visible and NIR wavelengths. The protostellar jets/outflows, however, can escape their dense envelopes, making it possible to study the outflow rates at optical and NIR wavelengths (e.g., B. Reipurth et al. 2002; M. Reiter & N. Smith 2013). Accretion-driven outflows and jets also play vital roles in shaping the initial mass function (IMF; e.g., D. Guszejnov et al. 2022; U. Lebreuilly et al. 2024). They can inject energy and momentum into the surroundings and disperse a significant fraction of the protostellar envelope, which limits star formation efficiency (e.g., S. M. Fall et al. 2010; A. Frank et al. 2014; S. S. R. Offner & H. G. Arce 2014; C. Federrath 2015; N. M. Habel et al. 2021; S. M. Appel et al. 2023).

Class 0 protostars have been extensively studied at (sub) millimeter wavelengths (e.g., P. Andre et al. 1993; T. L. Bourke et al. 2005; J. K. Jørgensen et al. 2007; J. Di Francesco et al. 2008; J. K. Jørgensen et al. 2009; Y. Matsushita et al. 2019; C.-F. Lee et al. 2021; L. Podio et al. 2021) and NIR/mid-IR (MIR; e.g., B. Reipurth et al. 2002; M. Reiter & N. Smith 2013; D. M. Watson et al. 2016; Y.-L. Yang et al. 2022; D. Harsono et al. 2023; N. G. C. Brunken et al. 2024; A. Caratti o Garatti et al. 2024; P. Nazari et al. 2024; K. Slavicinska et al. 2024; H. Tyagi et al. 2024). These observations have revealed the presence of highly collimated, fast-moving molecular jets and wide-angled, slow-moving molecular outflows originating from the vicinity of protostars, although molecular jets may not be universally detected toward all protostars (e.g., C.-F. Lee et al. 2017; C.-F. Lee 2020; T. P. Ray & J. Ferreira 2021; S. Dutta et al. 2023). Using isotopologues of CO and other dense gas tracers, the Atacama

Large Millimeter/submillimeter Array (ALMA) has detected the cool gas that dominates the mass of the outflow and is too cold to be detected by JWST. JWST has detected and mapped warm gas in accretion flows and outflow shocks (T. P. Ray et al. 2023; A. E. Rubinstein et al. 2024; J. D. Green et al. 2024; A. Caratti o Garatti et al. 2024) with an angular resolution comparable to ALMA. JWST has also detected the atomic jet (Y.-L. Yang et al. 2022; H. Beuther et al. 2023; D. Harsono et al. 2023; S. A. Federman et al. 2024; M. Narang et al. 2024) and direct signatures of accretion such as the H I lines (D. Harsono et al. 2023; S. A. Federman et al. 2024) and OH emission (D. A. Neufeld et al. 2024).

Cederblad (Ced) 110 IRS4 (eHOPS-cha-3) is a Class 0/I protostellar system ($L_{\rm bol} = 1.73\ L_{\odot}$, $T_{\rm bol} = 74$ K; R. Pokhrel et al. 2023a, 2023b;[5] see also N. Ohashi et al. 2023) in the Chamaeleon (Cha) I dark cloud (T. Prusti et al. 1991; M. Hiramatsu et al. 2007; T. A. van Kempen et al. 2009; P. Manoj et al. 2011) located at a distance of about 189 pc from Earth. Ced 110 IRS4 is the brightest object in the Ced 110 region (P. Persi et al. 2001) and is associated with NIR bipolar nebulosity (H. Zinnecker et al. 1999; P. Persi et al. 2001; K. M. Pontoppidan & C. P. Dullemond 2005). High-resolution ALMA observations of Ced 110 IRS4 have shown that the system is a binary consisting of Ced 110 IRS4A (R.A. = 11:06:46.369; decl. = −77:22:32.88) and Ced 110 IRS4B (R.A. = 11:06:46.772; decl. = −77:22:32.76) (N. Ohashi et al. 2023; J. Sai et al. 2023) with a projected separation of ∼1.″3 or 250 au. J. Sai et al. (2023) found that Ced 110 IRS4A has a stellar mass of 1.21–1.45 $M_{\odot}$ while Ced 110 IRS4B is a substellar companion with a mass of 0.02–0.05 $M_{\odot}$. They estimated the dust disk radii for Ced 110 IRS4A and IRS4B to be 91.7 ± 0.2 au and 33.6 ± 0.6 au, respectively. The disk masses are in the range of 38.85–97.43 $M_{\oplus}$ and 0.825–2.07 $M_{\oplus}$ for Ced 110 IRS4A and Ced 110 IRS4B, respectively. J. Sai et al. (2023) also suggested that the northern side of the disk might be the near side. The physical properties of the disks derived from the ALMA Early Planet Formation in Embedded Disks (eDisk) data are important for us to understand the outflow/jet observed with JWST.

Arc-like structures on the northern side of Ced 110 IRS4 at a radius of ∼1100 au (∼6″) were detected in the NIR by H. Zinnecker et al. (1999), P. Persi et al. (2001), and K. M. Pontoppidan & C. P. Dullemond (2005). The higher-resolution ALMA observations of several species, including $C^{18}O$ J = 2–1, SO $J_N = 6_5{-}5_4$, H_2CO, and c-C_3H_2, found similar structure and were able to study their kinematics and substructures with the high spatial and spectral resolution offered by the ALMA data (J. Sai et al. 2023).

The NIR/MIR emission from the Ced 110 IRS4 system has been studied with Spitzer (F. Lahuis et al. 2010; P. Manoj et al. 2011). These studies detected not only the gas-phase emission from [Fe II], [Ne II], and molecular H_2 but also strong absorption features at 6.0 μm due to H_2O ice; at 6.8 μm due to CH_3OH, NH_4^+, and strongly polar H_2O ice; and at 15.2 μm due to CO_2 ice along with the 10 μm silicate feature. These observations, however, lacked both the resolution and the sensitivity to spatially map these features.

Recently, W. R. M. Rocha et al. (2025) carried out a detailed analysis of the ice features seen toward Ced 110 IRS4A and IRS4B using JWST Near Infrared Camera (NIRCam) Wide-Field Slitless Spectroscopy (WFSS), the Near InfraRed Spectrograph (NIRSpec), and Mid-Infrared Instrument (MIRI) Medium Resolution Spectroscopy (MRS). They found that the ice abundances for Ced 110 IRS4A and IRS4B were similar to the starless regions in the same molecular cloud, and both protostars showed hints of thermal processing of ices. This study, however, did not analyze the gas-phase emission from the system.

Despite multiple submillimeter observations of Ced 110 IRS4 (M. Hiramatsu et al. 2007; T. A. van Kempen et al. 2009; J. Sai et al. 2023), no definitive signatures of outflows or jets have been detected from the system. Moreover, the rich gas-phase spectra observed toward the two protostars (W. R. M. Rocha et al. 2025) necessitate further investigation. To better understand the structure revealed by ALMA submillimeter observations (both continuum and molecular line emission) and the scattered light morphology and to resolve whether Ced 110 IRS4 is associated with a jet or a wide-angle outflow, we conducted a joint analysis using ALMA and JWST observations.

Our study leverages high-resolution imaging from JWST's NIRCam (L. W. Huff 2005) and MRS integral field unit data from MIRI (G. H. Rieke et al. 2015; G. S. Wright et al. 2015). These data sets (M. K. McClure et al. 2023; W. R. M. Rocha et al. 2025) enable a systematic examination of NIR and mid-infrared (MIR) jet and outflow kinematics and morphology in the Ced 110 IRS4 region, traced through atomic and fine-structure (FS) lines and molecular H_2. A detailed analysis of the mass accretion and outflow rates will be presented in M. Narang et al. (2025, in preparation). In Section 2, we describe the JWST and ALMA observations and the data reduction process. Section 3 presents our analysis of the large-scale outflow structures and the morphology of the inner ∼1000 au surrounding the protostar. Section 4 discusses the implications of our findings, and Section 5 summarizes the study's conclusions.

2. Observations and Data Reduction

2.1. JWST Observations

The NIRCam and MIRI MRS observations of Ced 110 IRS4 were carried out as part of the JWST Director's Discretionary Early Release Science Program IceAge: Chemical Evolution of Ices during Star Formation (Program ID 1309; PI Melissa McClure, Adwin Boogert, Harold Linnartz—in memoriam; M. K. McClure et al. 2023; W. R. M. Rocha et al. 2025). The NIRCam imaging was carried out with the F140M, F150W, and F410M filters. The NIRCam reduction was carried out using the default reduction script. The data were reduced using the pipeline version 1.14.0 and the JWST Calibration References Data System context version jwst_1242.pmap. The NIRCam images have an empirical FWHM of 0.″046, 0.″049, and 0.″133 for the F140M, F150W, and F410M filters, respectively.[6]

The MIRI MRS observations of Ced 110 IRS4 were carried out on 2023 July 12, almost a year after the NIRCam observations. Ced 110 IRS4 was observed using all four channels of MIRI MRS. Each channel was exposed for 1665 s, using the "FASTR1" readout pattern with 150 Groups/Int and with a single integration. The data were then reduced using the JWST pipeline, version 1.14.1.dev49+g9e857a52, and the calibration file CRDS jwst_1215.pmap. The MIRI data were reduced using the standard Stage-1 JWST pipeline Detector1Pipeline to reduce the MIRI

[5] irsa.ipac.caltech.edu/data/Herschel/eHOPS/overview.html

[6] https://jwst-docs.stsci.edu/jwst-near-infrared-cameranircam-performancenircam-point-spread-functions

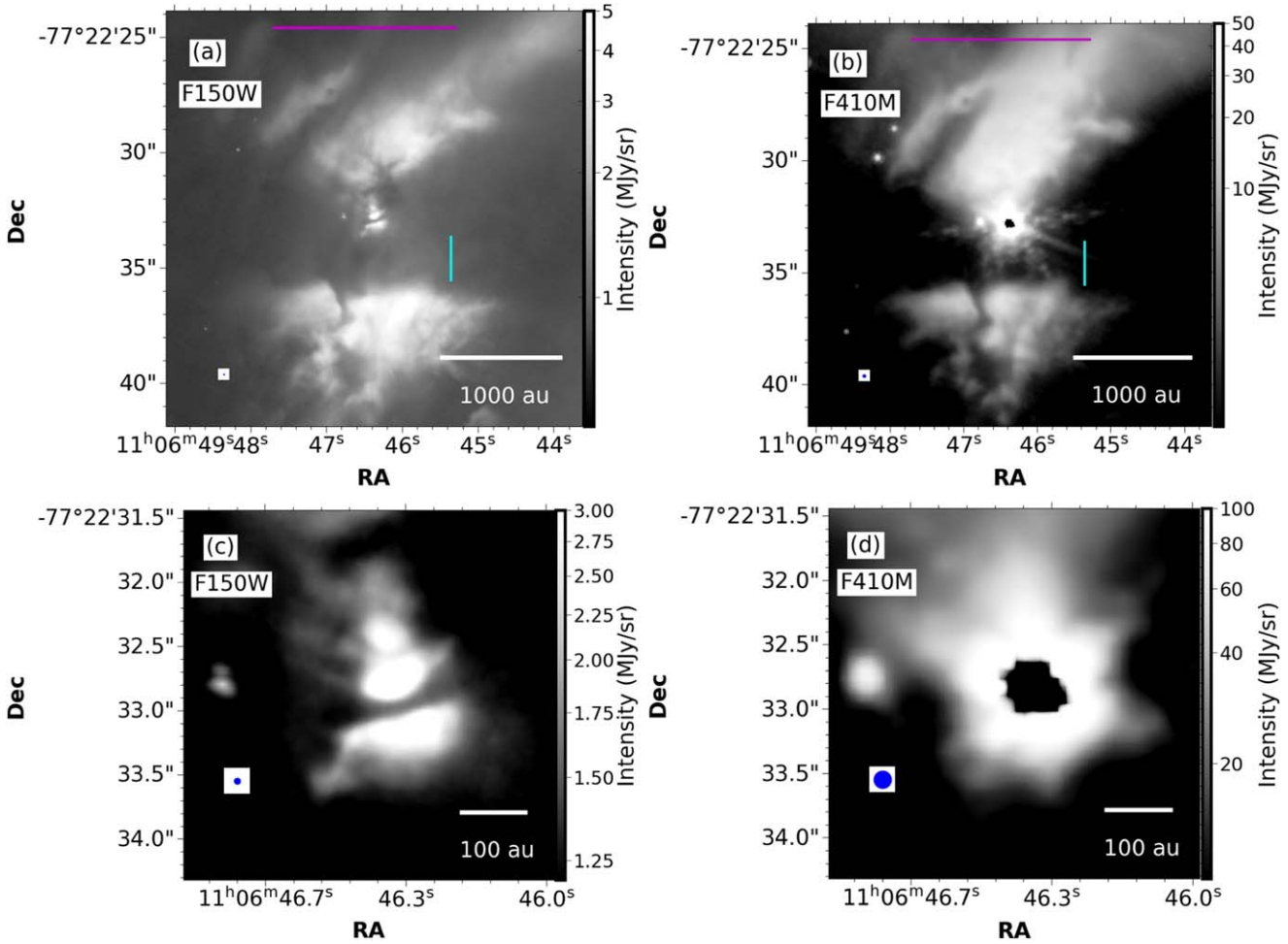

Figure 1. The NIRCam F150W and F410M filter image of the Ced 110 IRS4 region in gray scale. The NIRCam FWHM is shown in the lower left corner in blue. The scale bar in white is also shown in the lower right corner. The beam sizes are given in Table 2. The arc-like structure is marked with a magenta line, and the dark band is marked with a cyan line. The same intensity scaling is followed in Figure 2 for the NIRCam observations.

MRS data starting from uncal data, followed by the Stage-2 JWST pipeline Detector2Pipeline. The Stage-3 Spec3Pipeline step was run with the CubeBuildStep set to "band" mode such that each channel and each band are reduced as a separate fits file. Although most cosmic-ray events are flagged and rejected during the Stage-1 process while constructing the uncalibrated slope image, some outliers still manage to pass through both Stage-1 and Stage-2.[7] Therefore, we also turned on the outlier detector in Stage-3, which helped remove many of the artifacts from the spectral cube.

2.2. ALMA Observations

The ALMA observations of Ced 110 IRS4 were carried out during ALMA's Cycles 7 and 8 at ALMA Band 6 with antenna configurations of C-5 and C-8, as a part of the ALMA large program eDisk (2019.1.00261.L: PI N. Ohashi N. Ohashi et al. 2023). An overview of the data and first results about Ced 110 IRS4 from the ALMA eDisk observations were presented by N. Ohashi et al. (2023) and J. Sai et al. (2023). Thus, we will only present a brief overview of the observational setup and data reduction. CO isotopologues, SO, and other molecular lines were observed using Frequency Division Mode (FDM). The 1.3 mm (225 GHz) continuum emission was extracted from the line-free channels of the spectral windows, with a maximum window width of 1.875 GHz. The ALMA data were reduced with the Common Astronomy Software Applications package CASA 6.2.1 (J. P. McMullin et al. 2007). We made Short-Baseline + Long-Baseline (SBLB) continuum images and both Short-Baseline (SB) and SBLB images for the line emission from the Ced 110 IRS4 region for varying robust values. The details of the imaging procedure can be found in N. Ohashi et al. (2023) and J. Sai et al. (2023). We have listed the parameters (robust value, beam size, and beam position angle) for the various maps used in this work in Table 1.

Since we are comparing data from ALMA and JWST in this work, we assessed the offset between ALMA and JWST images by measuring the position of Ced 110 IRS4B. For the NIRCam observations we used the F410 filter. Due to the disk shadow present in the F150 filter (see Figures 1 and 2), it was more challenging to accurately measure the position in that band. We did not measure the position of IRS4A, as it was saturated. The offset between the NIRCam image and ALMA was found to be approximately 0.″055, which is less than 1 pixel (pixel scale for F410M 0.″063 pixel^{-1}), indicating an excellent positional match between NIRCam and ALMA observations.

The MIRI MRS channel-1 observations of Ced 110 IRS4B have contamination from the MIRI MRS point-spread function

[7] https://jwst-docs.stsci.edu/jwst-science-calibration-pipeline/Stages-of-jwst-data-processing/calwebb_spec3#gsc.tab=0

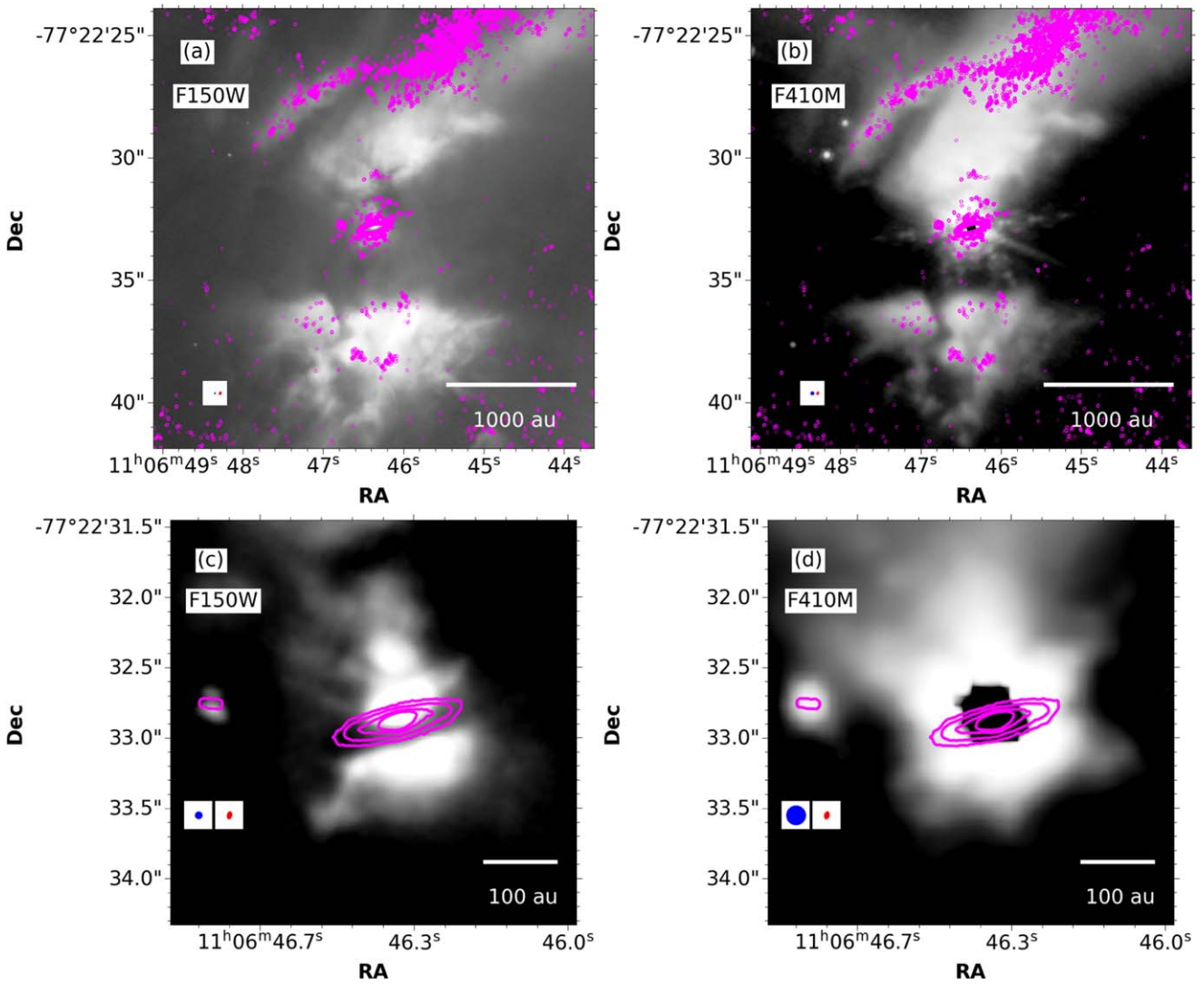

Figure 2. The NIRCam F150W and F410M filter image of the Ced 110 IRS4 region in gray scale is shown, with the ALMA 1.3 mm continuum map overlaid as magenta contours. The 1.3 mm continuum maps, with robust parameters of 2.0 and 0.0, are overlaid on the wide and zoomed-in views of the NIRCam image, respectively. The contours are 3σ, 10σ, 30σ, 70σ, and 100σ, with $\sigma_{\rm robust\,=\,2}$ = 14 μJy and 10σ, 30σ, 70σ, and 100σ with $\sigma_{\rm robust\,=\,0}$ = 16 μJy. The NIRCam FWHM and the ALMA beams are shown in the lower left corner as blue and red ellipses, respectively. The scale bar in white is also shown in the lower right corner. The beam sizes and PA are given in Tables 1 and 2.

(PSF) of Ced 110 IRS4A, and beyond channel 8 μm the emission from Ced 110 IRS4B drops. Furthermore, at shorter wavelengths the contribution from scattered light emission is also high. Therefore, we have opted to use the 14.14 μm emission from Ced 110 IRS4A to investigate the positional offset between the JWST MIRI and ALMA positions. The MIRI 14.14 μm continuum position of Ced 110 IRS4A differed from the ALMA 1.3 mm continuum position by 0.″2 (the pixel scale for MIRI 14.14 μm is 0.″2 pixel^{-1}). To address this, we corrected the astrometry of the MIRI MRS observations by shifting the 14.14 μm continuum position of the protostar to align with the ALMA 1.3 mm continuum position.

3. Results

3.1. Continuum Emission with NIRCam and MIRI MRS

Previous NIR observations of Ced 110 IRS4 (K. M. Pontoppidan & C. P. Dullemond 2005) have shown the existence of a bipolar structure separated by a dark band and a bright central source. However, those observations were limited to a resolution of 0.″7, much larger than the ALMA eDisk (see Table 1) or the NIRCam IceAge observations. To explore the large-scale structure around the Ced 110 IRS4 system, we analyzed the NIRCam F150W and F410M observations alongside ALMA continuum and CO isotopologue data.

Figure 1 shows the NIRCam observations of the Ced 110 IRS4 region in F150W and F410M filters. In Figures 1(c) and (d), we present a close-up view of the Ced 110 IRS4 region, focusing on the inner ∼3″ region. The NIRCam observations detect not only Ced 110 IRS4A but also Ced 110 IRS4B. The NIRCam images (at large scales; Figures 1(a) and (b)) show bipolar nebulosity with lobes and arc-like structures separated by a dark band that is ∼2.″5 wide. This arc-like structure observed in NIRCam is also detected in the 1.3 mm continuum map (Figures 2(a) and (b)). We also see a bow shock toward the south of the protostars, associated with a craved gap in the nebulosity.

The zoomed-in JWST NIRCam F150W (Figure 1(c)) shows a dark lane passing through both Ced 110 IRS4A and IRS4B.

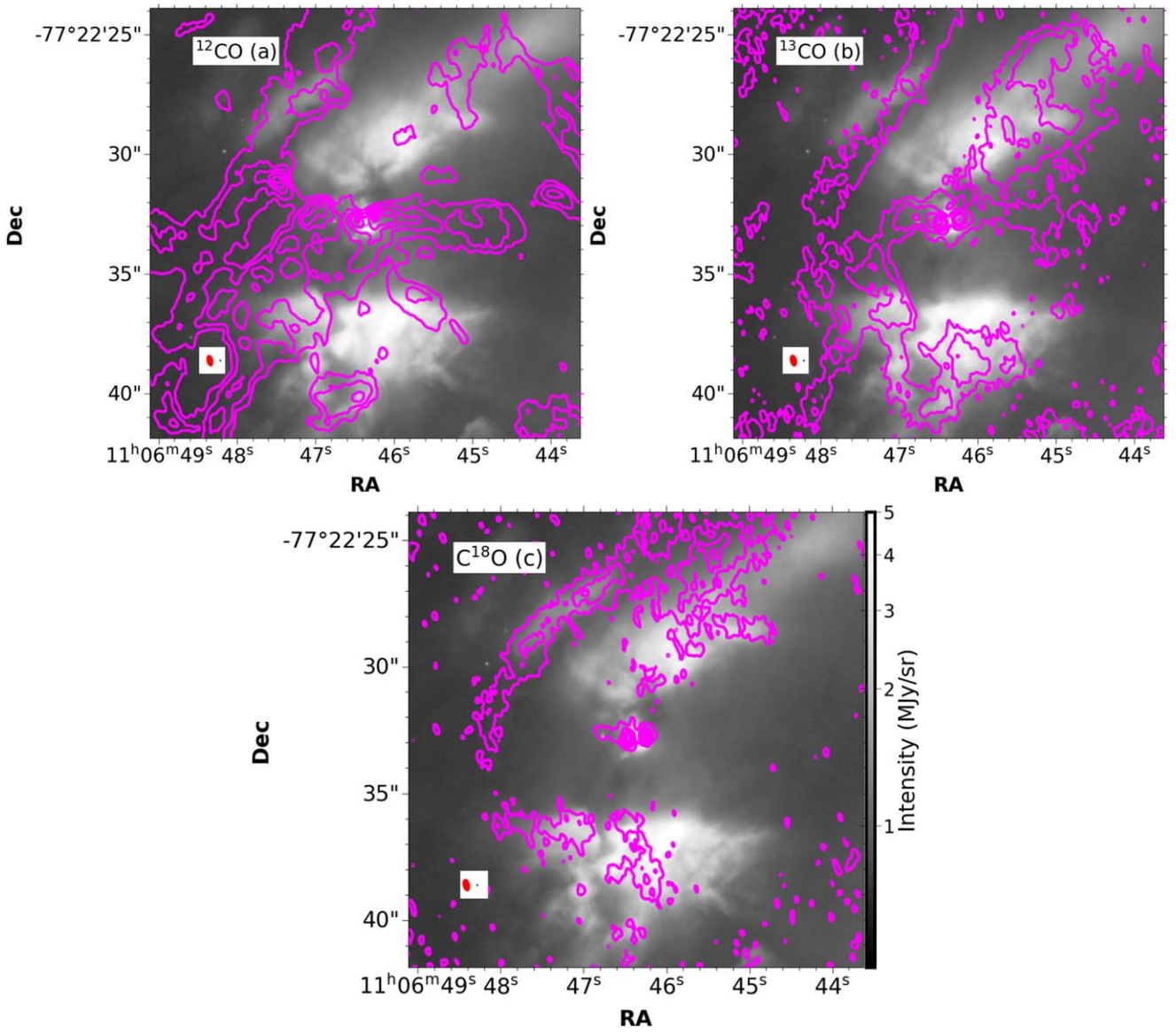

Figure 3. The NIRCam F150W filter image of the Ced 110 IRS4 region, with the ALMA (SB) CO isotopologue integrated intensity image overlaid as magenta contours. The contours for ^{12}CO and ^{13}CO are 15%, 30%, 50%, 70%, 90%, and 99% $\times F_{\rm max}$, where $F_{\rm max}$ for ^{12}CO is 0.36 Jy beam^{-1} km s^{-1}; $F_{\rm max}$ for ^{13}CO is 0.17 Jy beam^{-1} km s^{-1}. The contours for C^{18}O are 30%, 50%, 70%, 90%, and 99% $\times F_{\rm max}$, where $F_{\rm max}$ for C^{18}O is 0.07 Jy beam^{-1} km s^{-1}. The NIRCam FWHM and the ALMA beams are shown in the lower left corner as blue and red ellipses, respectively. The beam sizes and PA are given in Tables 1 and 2. All NIRCam images have the same intensity scale.

The dark lane represents the disk shadow from the nearly edge-on disk around each protostar. This also indicates that Ced 110 IRS4B has a nearly edge-on inclination, similar to Ced 110 IRS4A and consistent with what was found by J. Sai et al. (2023). We further find that the NIRCam F150W emission is also extended toward the north in the direction of the jet (see Section 3.2 and Figure 8). Within the wavelength range of the F150W filter, there are several transitions of [Fe II] lines that have been detected with JWST. These [Fe II] lines trace the atomic jet from the protostar (e.g., K. Assani et al. 2024), which can be used to determine the outflow rate from the jet. The emission from Ced 110 IRS4A is, however, saturated in F410M (Figure 1(d)), thus making it difficult to analyze.

To investigate the relationship between the disk shadow and the dust disk at 1.3 mm, we overlaid the ALMA continuum image onto the zoomed-in JWST NIRCam F150W and F410M images (Figures 2(c) and (d)). We observed excellent positional alignment between the NIRCam and ALMA data for both protostars. The zoomed-in NIRCam F150W view of Ced 110 IRS4A and IRS4B (Figure 2(c)) reveals that the ALMA continuum disk aligns with the dark lanes corresponding to the disk shadow, though the ALMA disk is slightly shifted to the northern side. This slight shift might be because the northern side of the disk, which is the near side, is brighter than the southern side and/or due to the opacity of dust in the midplane at 1.5 μm and 1.3 mm being different.

In Figure 3 we compare the large-scale structure seen in the JWST NIRCam F150W images with the CO isotopologues from the ALMA observations. J. Sai et al. (2023) have shown that the CO isotopologues trace both the large-scale structure and the Keplerian disk around Ced 110 IRS4. Upon overlaying the ALMA CO (SB) isotopologue data on the NIRCam images, we observe that the large-scale structures traced are best traced in C^{18}O, which align well with the F150W emission. The

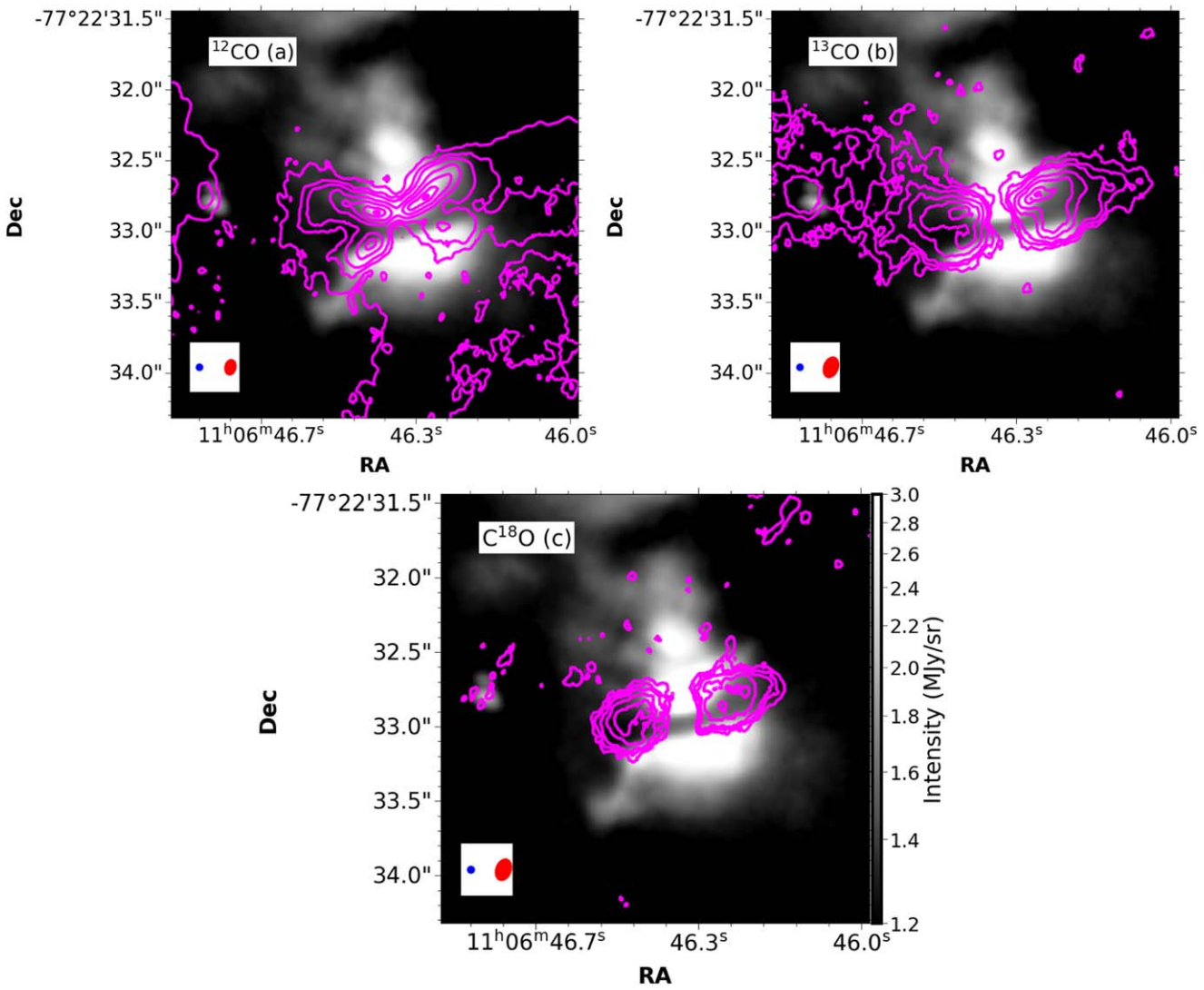

Figure 4. The NIRCam F150W filter image of the Ced 110 IRS4 region, with the ALMA (SBLB) CO isotopologue integrated intensity image overlaid as magenta contours. The contours for are 15%, 30%, 50%, 70%, 90%, and 99% × F_{max}, where F_{max} for ^{12}CO is 150 mJy beam^{-1} km s^{-1}; F_{max} for ^{13}CO is 60 mJy beam^{-1} km s^{-1}, and F_{max} for C^{18}O is 30 mJy beam^{-1} km s^{-1}. The NIRCam FWHM and the ALMA beams are shown in the lower left corner as blue and red ellipses, respectively. The beam sizes and PA are given in Tables 1 and 2. All NIRCam images have the same intensity scale.

northern arc-like structure and the southern structures are partially traced in all CO isotopologues. The ^{13}CO also traces the apparent bow shock at the end of the southern lobe.

In Figure 4, we present a zoomed-in view of the ALMA SBLB data of CO isotopologues overlaid on the NIRCam F150W image. The gas disk, as traced by CO emissions (J. Sai et al. 2023), aligns with the disk shadow observed in the NIRCam data. This alignment underscores the powerful synergy between high-resolution ALMA and NIRCam observations, demonstrating how combining these data sets can enhance our understanding of the structure and dynamics of protostellar disks. The gas disk similar to the 1.3 mm dust also appears to be slightly shifted toward the north from the shadow.

The MIRI MRS continuum images for Ced 110 field are shown in Figure 5. We made continuum-integrated images at 5.38 μm (by integrating from 5.35 to 5.4 μm) and at 14.14 μm (by integrating from 14.1 to 14.18 μm). Ced 110 IRS4A is clearly detected in both images, while Ced 110 IRS4B is weakly detected only at 5.38 μm, with strong contamination from the PSF of Ced 110 IRS4A. However, we do not detect Ced 110 IRS4B at 14.14 μm.

3.2. Morphology of the Atomic Jet

The JWST MIRI observations of Ced 110 IRS4 trace the atomic jets and molecular outflow structures down to scales of ∼50 au, comparable to the spatial resolution of ALMA observations. J. Sai et al. (2023) reported a complex emission profile around the source, with no discernible jets or outflows detected in ^{12}CO, SO, and SiO emission. Four transitions of the [Fe II] lines were detected toward Ced 110 IRS4 (see Table 3). The line maps (based on continuum-subtracted integrated line intensity) for these transitions are shown in Figure 6. The [Fe II] lines trace the atomic jet launched from the vicinity of Ced 110 IRS4A, marking the first detection of a jet from this source. There are hints of weak [Fe II] emission from Ced 110 IRS4B, especially at longer wavelengths, but because of the poorer spatial resolution, it is difficult to separate the emission between Ced 110 IRS4A and Ced 110 IRS4B. In Table 3 we have listed the flux extracted from Ced 110 IRS4A and Ced 110 IRS4B with a radius equal to the MIRI MRS FWHM (based on D. D. Law et al. 2023) at that wavelength. We have also overlaid the 1.3 mm continuum emission on top of the

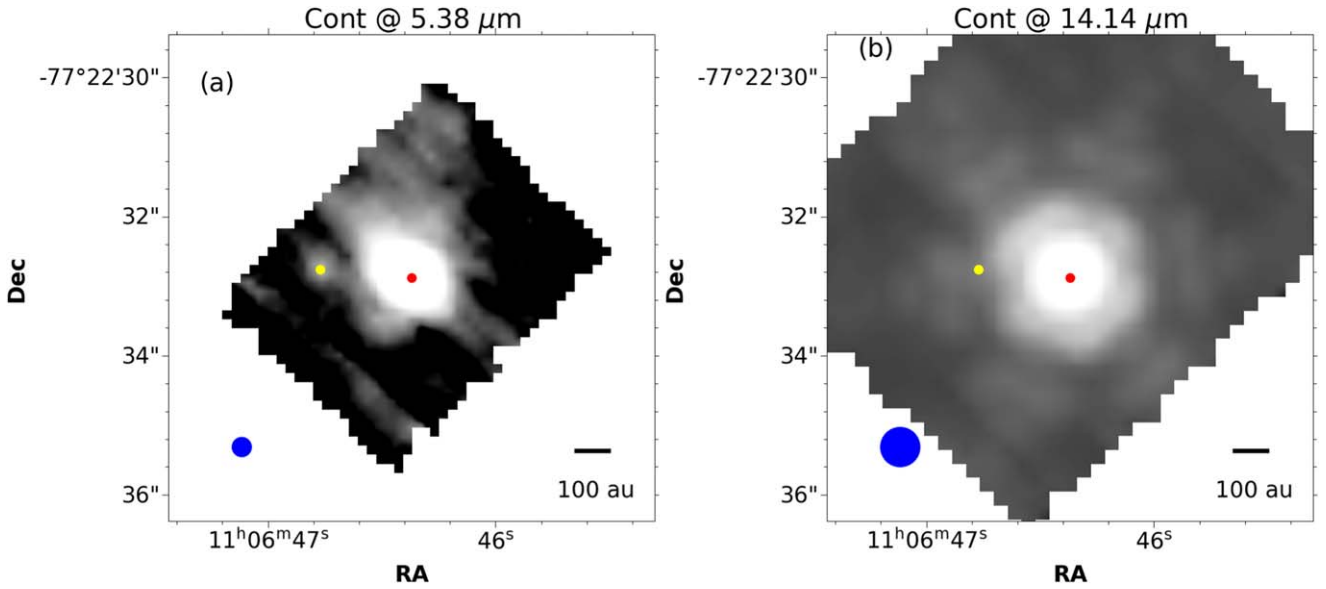

Figure 5. The MIRI MRS continuum image of the Ced 110 IRS4 region in gray scale. The ALMA 1.3 mm position for Ced 110 IRS4A is shown as a red circle, and that for IRS4B is shown as a yellow circle. The scale bar corresponding to 100 au is shown in the lower right corner. The MIRI FWHM based on D. D. Law et al. (2023) is shown in the lower left corner as a blue circle.

[Fe II] emission. The jet from Ced 110 IRS4A is perpendicular to the disk. The [Fe II] jet (as traced in the 5.34 μm line) appears to be much smaller than the disk diameter.

The jet expands as it moves away from the driving source, with the expansion being most evident in the [Fe II] line at 5.34 μm owing to its higher angular resolution. We find that the northern part of the jet is brighter than the southern part, potentially indicating different excitation conditions or levels of extinction. J. Sai et al. (2023) also suggested that the northern side of the protostar was aligned toward us; part of this brightness asymmetry therefore can also be attributed to the geometry.

In Figure 7, we show the line maps of some of the FS lines detected toward Ced 110 IRS4. We have listed the line flux (extracted from the aperture shown in Figure 7) from the FS lines in Table 3. The atomic and FS jet detected from Ced 110 IRS4B based on the line flux is about an order of magnitude fainter than that detected from Ced 110 IRS4A. The jet is prominently detected in the [Ne II] line at 12.81 μm and appears to be brighter on the northern side, similar to the [Fe II] jet (see Figure 6). However, in other FS lines, such as [Ni II] at 6.63 μm and [Ar II] at 6.98 μm, the jet appears weaker and more concentrated around the central protostar. The [S I] emission at 25.25 μm is detected only at the central protostar. The emission detected in the [Ne II] line (Figure 7) appears more extended than the disk, which reflects the poorer angular resolution (0.″53 or 100 au) of MIRI at this wavelength compared to ALMA continuum observations (0.″054 × 0.″035 or ∼10 au). We also find that the disk from Ced 110 IRS4B is also smaller than the emission detected in [Ar II] at 6.99 μm and [Ne II] at 12.81 μm. This could, again, be due to poorer resolution of JWST (0.″28–0.″53 or 53–100 au) as compared to the ALMA resolution.

We next compared the F150W NIRCam observations with the jet detected in [Fe II] at 5.34 μm and [Ne II] at 12.81 μm (see Figure 8). We find that the emission seen in the F150W filter extends along the direction of the jet detected from the protostar, particularly toward the north. We do not find a strong correlation between the jet, as traced by FS lines, and the large-scale structures observed in the NIRCam and ALMA data. Notably, a portion of the F150W emission near Ced 110 IRS4A overlaps with the jet detected from the protostar. However, since the MIRI observations of the jet cover only a small fraction of the NIRCam and ALMA field of view (FOV), additional observations are needed to confirm the validity of this conclusion.

3.3. Jet Width

At 5.34 μm the FWHM of the PSF of MIRI MRS is 0.″282 (D. D. Law et al. 2023) or ∼53 au (at the distance of Ced 110 IRS4). Given the small PSF of the instrument, it is possible to measure the jet width as a function of distance from the protostar. We find that the [Fe II] at 5.34 μm has a goblet-like morphology, i.e., a long narrow neck that opens and expands rapidly as we move away from the central source. Therefore, to quantify this expansion and determine the opening angle of the protostellar jet, we measure the jet width as a function of distance from the protostar.

To measure the jet width, we use slices perpendicular to the jet axis (see M. Narang et al. 2024). Given the pixel size of 0.″13 and the FWHM of the PSF of MIRI MRS of 0.″282, we opted to average over 3 pixels. These slices are shown in Figure 9(a) and are aligned perpendicular to the jet. Only the jet's inner ∼400 au lies completely within the MIRI FOV. In Figure 9(b) we show the observed jet width as a function of distance from the protostar. The observed width of the jet is smoothened by the 0.″282 owing to the MIRI MRS PSF. Therefore, we subtract out (in quadrature) the broadening due to the PSF from the jet width to measure the deconvolved jet width. In Figure 9(b) we then also show the deconvolved jet width as a function of distance from the protostar.

As shown in Figure 9(b), not only does the jet rapidly expand moving away from the center, but its opening angle, Θ (where $\Theta = \frac{1}{2}\tan^{-1}\left(\frac{\text{Deconvolved jet width}}{\text{Distance from the central source}}\right)$), also varies. The deconvolved jet width in the central region is $\leqslant 51 \pm 8.6$ au. However, this measurement represents only an upper limit to the jet width owing to the limited resolution of the MIRI MRS instrument. Notably, however, this width is significantly smaller than the

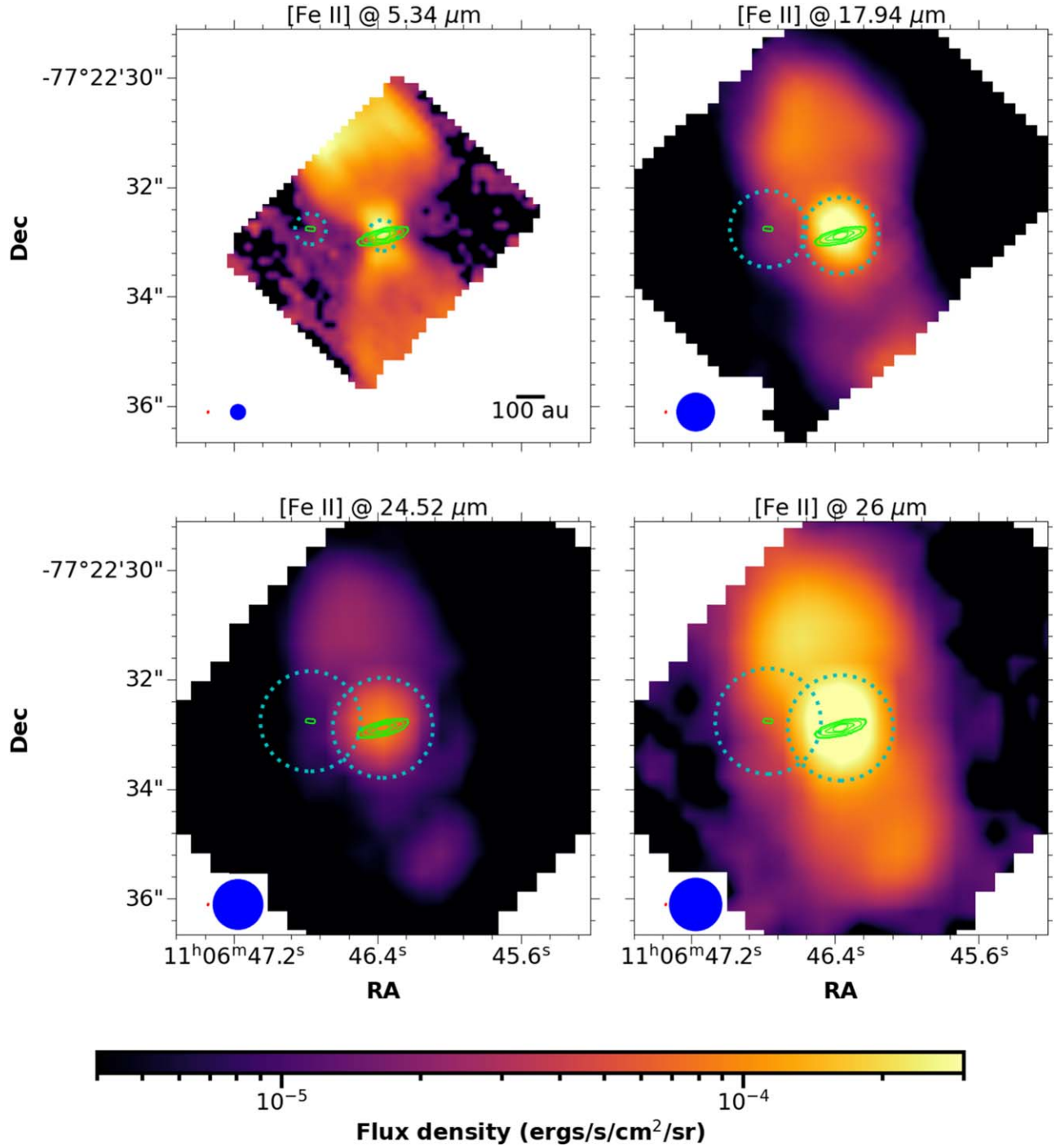

Figure 6. The morphology of the [Fe II] lines detected toward Ced 110 IRS4. All images are cropped to the same spatial scale of $7''.2 \times 7''.2$ and have the same color scale. The ALMA 1.3 mm contours are shown in lime. The scale bar corresponding to 100 au is shown in the lower right corner. The MIRI MRS FWHM based on D. D. Law et al. (2023) is shown in the lower left corner as a blue circle, and the ALMA beam is shown in red. We also show in cyan apertures (radius = MIRI MRS FWHM) used to extract line flux from the two protostars.

disk diameter of 183.4 ± 0.4 au, as reported by J. Sai et al. (2023), where the dust disk radius encloses 90% of the flux density. Additionally, the average opening angle within the inner 150 au of the protostar (by fitting the deconvolved jet width as a function of distance) is calculated to be 23° ± 4°.

3.4. Kinematics of the Atomic Jet

To explore the velocity structures within the jet, we analyzed the [Fe II] line at 5.34 μm. This line offers the best velocity and spatial resolution along all FS lines detected within the MIRI MRS range. In Figure 10 we show the moment 1 map of the 5.34 μm [Fe II] for Ced 110 IRS4. We find that the northern jet exhibits a blueshifted velocity with respect to the systemic velocity (of 4.67 km s^{-1}; J. Sai et al. 2023), while the southern jet displays a redshifted velocity. This means that the northern part of the protostar faces toward us, similar to the conclusion from J. Sai et al. (2023) based on the disk brightness asymmetry. The velocity of the jet on both sides is fairly

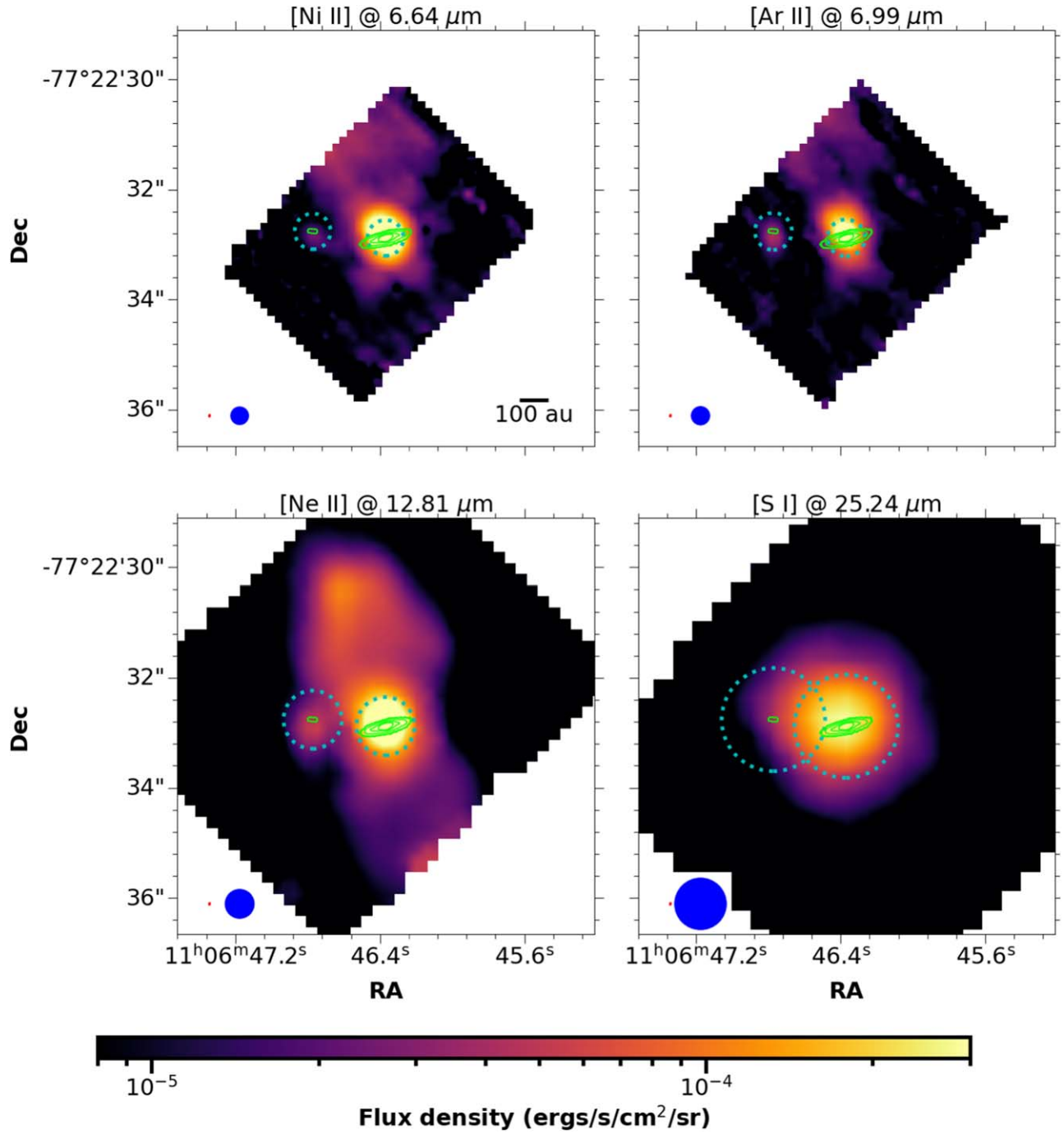

Figure 7. The morphology of the atomic FS lines detected toward Ced 110 IRS4. All images are cropped to the same spatial scale of $7''.2 \times 7''.2$ and have the same color scale. The ALMA 1.3 mm contours are shown in lime. The scale bar corresponding to 100 au is shown in the lower right corner. The MIRI MRS FWHM based on D. D. Law et al. (2023) is shown in the lower left corner as a blue circle, and the ALMA beam is shown in red. We also show in cyan apertures (radius = MIRI MRS FWHM) used to extract line flux from the two protostars.

constant, and the bulk blueshift and redshift velocity is $\sim$30–40 km s^{-1}. This is much larger than the systemic cloud velocity, as well as the velocity of the cold gas detected with ALMA. J. Sai et al. (2023) found that the blueshifted and redshifted emissions detected from molecular CO and SO both had a relatively small velocity of $\pm$4 km s^{-1} with respect to the systemic cloud velocity.

To further investigate the velocity structure of the jet, we constructed a position–velocity (PV) diagram for the [Fe II] line at 5.34 μm. For each slice of the spectral cube, we computed the velocity by converting the wavelength shift with respect to the lab wavelengths (B.-C. Koo et al. 2016; S. S. Tayal & O. Zatsarinny 2018) to a velocity shift. We meticulously chose a rectangular region that included the majority of the jet and only included the regions that were fully in the FOV, thus ensuring that no vital parts were excluded from the analysis (see Figure 11(a)). This rectangle region has a width of $1''.4$ and a length of $\sim 3''$. We further assume that the velocity of the jet

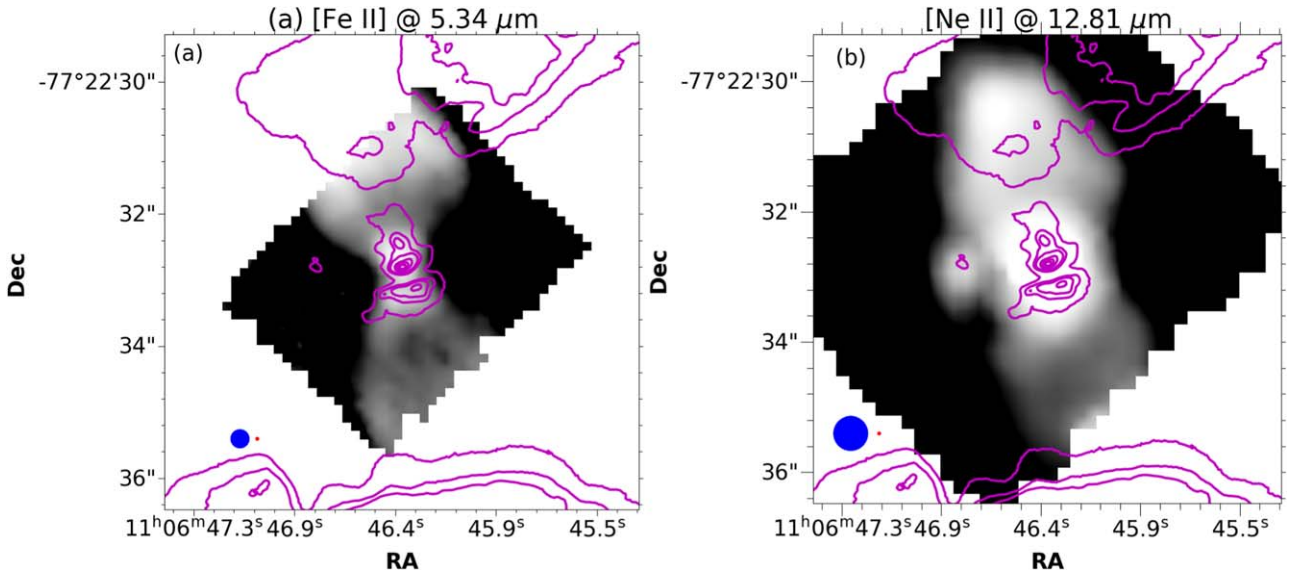

Figure 8. The atomic jet has traced in [Fe II] at 5.34 μm and [Ne II] at 12.81 μm, with NIRCam F150W emission overlaid on top in magenta. The MIRI FWHM based on D. D. Law et al. (2023) is shown in the lower left corner as a blue circle, while the NIRCam FWHM is shown as a red circle.

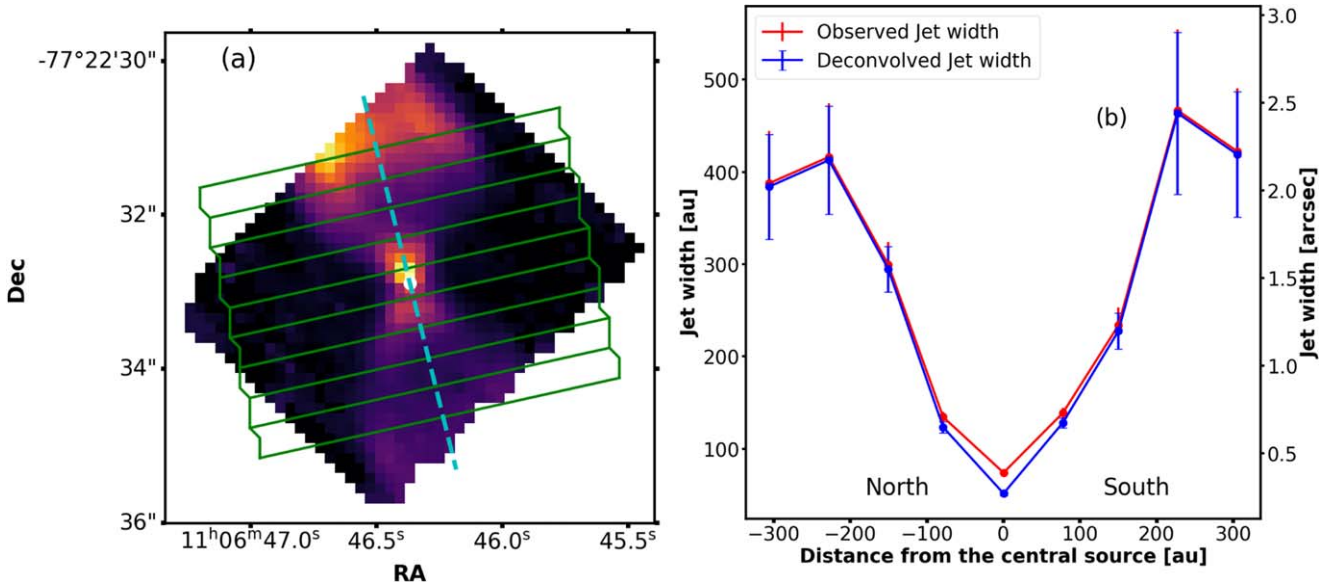

Figure 9. (a) The horizontal slices in green marked on top of the jet traced in [Fe II] at 5.34 μm. The white circle represents the protostellar position. The cyan dashed line marks the jet axis, which is perpendicular to the disk as traced in ALMA dust continuum. (b) The observed (in red) and deconvolved (in blue) jet width (FWHM) of the jet as a function of distance from the central protostar. The negative distance corresponds to the northern side, and the positive distance corresponds to the southern side.

is symmetric and set the average velocity of the jet to be zero. In Figure 11(b), we show the PV diagram for the [Fe II] line at 5.34 μm. We find that the peak-to-peak velocity of the jet is $\sim$60 km s^{-1}. Therefore, we take the velocity of the jet to be 30 km s^{-1}. The inclination angle of the protostellar disk is 76° (based on the dust disk morphology fitting by J. Sai et al. 2023). If we correct the jet velocity for the inclination, we find that the true velocity of the [Fe II] jet at 5.34 μm is $\sim$124 km s^{-1}, assuming that there is no additional radial shock component along our line of sight.

3.5. Morphology of the Molecular H_2 Outflow

The jets and wide-angle winds launched by the disks of the protostars sweep up the infalling envelopes, entraining gas along with them. In the swept-up gas, molecular H_2 gets heated in turbulent shocks. Therefore, by investigating the distribution of molecular H_2 emission, we can understand the morphology of the shock-heated gas that is entrained in the protostellar outflow. We detect several pure rotational transitions of H_2 0–0 S lines (see Figure 12) from H_2 0–0 S(1) to H_2 0–0 S(8) (see Table 4). The molecular H2 outflow displays a distinct morphology resembling two bowls or hemispheres placed back-to-back, in stark contrast to the hourglass-like shape typically seen in protostellar outflows (e.g., S. A. Federman et al. 2024; B. Nisini et al. 2024). The back-to-back hemisphere-like structure gets narrower and shows a neck at the position of IRS4A. The H_2 emission has minima at the neck position. In addition to the H_2 0–0 S lines, the H_2 1–1 S lines

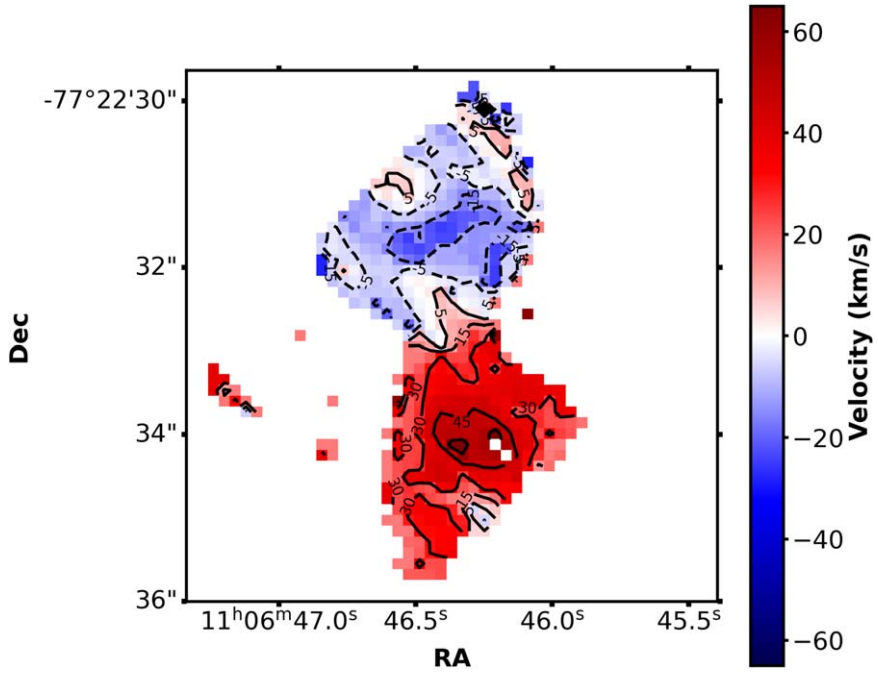

Figure 10. The moment 1 map for the [Fe II] line at 5.34 μm. The contours mark the velocities in km s^{-1}.

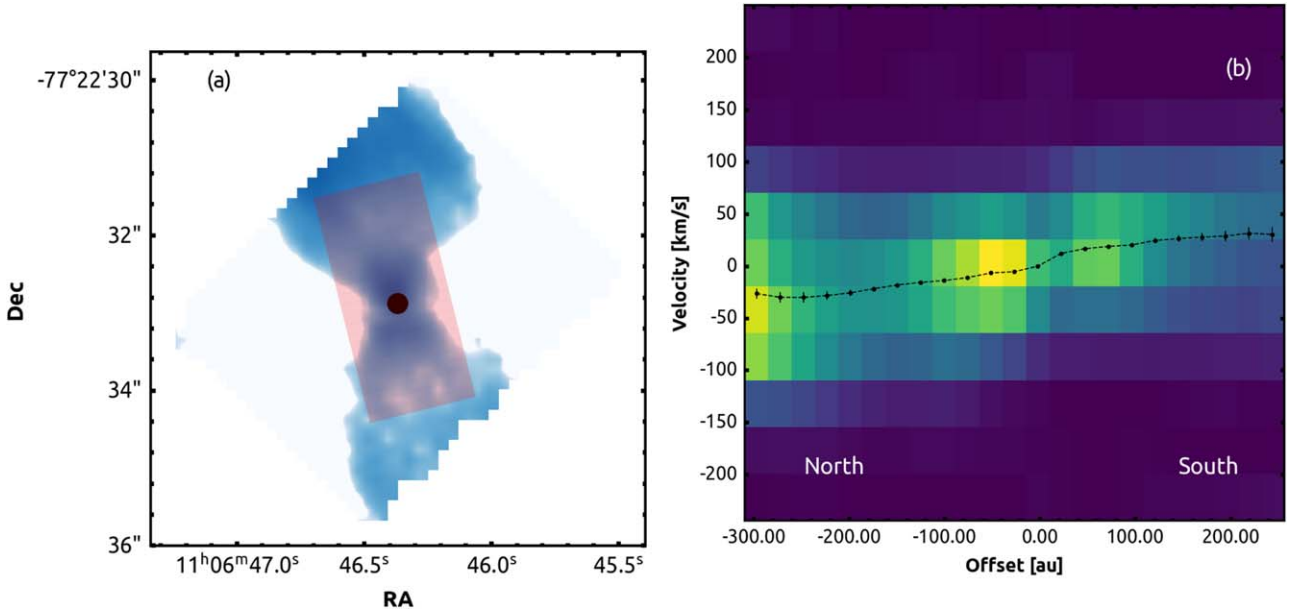

Figure 11. (a) The [Fe II] jet at 5.35 μm shown in blue, overlaid with a red rectangle that denotes the region considered for making the PV diagram. The black filled circle is the ALMA continuum position. (b) The PV diagram for the [Fe II] line at 5.34 μm as a function of the distance from the central protostar along the jet axis.

from S(3) to S(7) arising from the inner 2.″4 region around Ced 110 IRS4 are also detected. However, these lines are much weaker in strength as compared to the H_2 0–0 S transitions, and hence we do not analyze these lines in this work.

In Figure 13(a) we compared the NIRCam F150W image with the H_2 S(7) outflow. We find that the disk shadow as traced in NIRCam F150W aligns wells with the neck (the narrow part of the outflow that connects both hemispheres) in the F150W emission. In Figure 13(b), we show the H_2 S(7) line with the 1.3 mm overlaid on top. We find that the protostellar disk lies in the narrowest part of the neck between the two outflow hemispheres but slightly shifted toward the northern side. This is consistent with the outflow geometry with the near side on the northern side. The width of the H_2 at the neck of the emission is comparable to the continuum disk (see Section 4.2).

The ^{12}CO emission appears to trace the upper layers of the disk and disk rotation (J. Sai et al. 2023). The molecular ^{12}CO emission from the protostar shows four intensity peaks around Ced 110 IRS4A and a dark lane along the continuum major axis. The four intensity peaks likely come from a hotter disk surface on the near side and a colder disk inner surface on the far side of the disk (K. A. Rosenfeld et al. 2013; C. Pinte et al. 2018; J. Sai et al. 2023). On overplotting the ^{12}CO on the molecular H_2 emission (Figure 13(c)), we find that four intensity peaks in ^{12}CO line up with the base of the emission of molecular H_2.

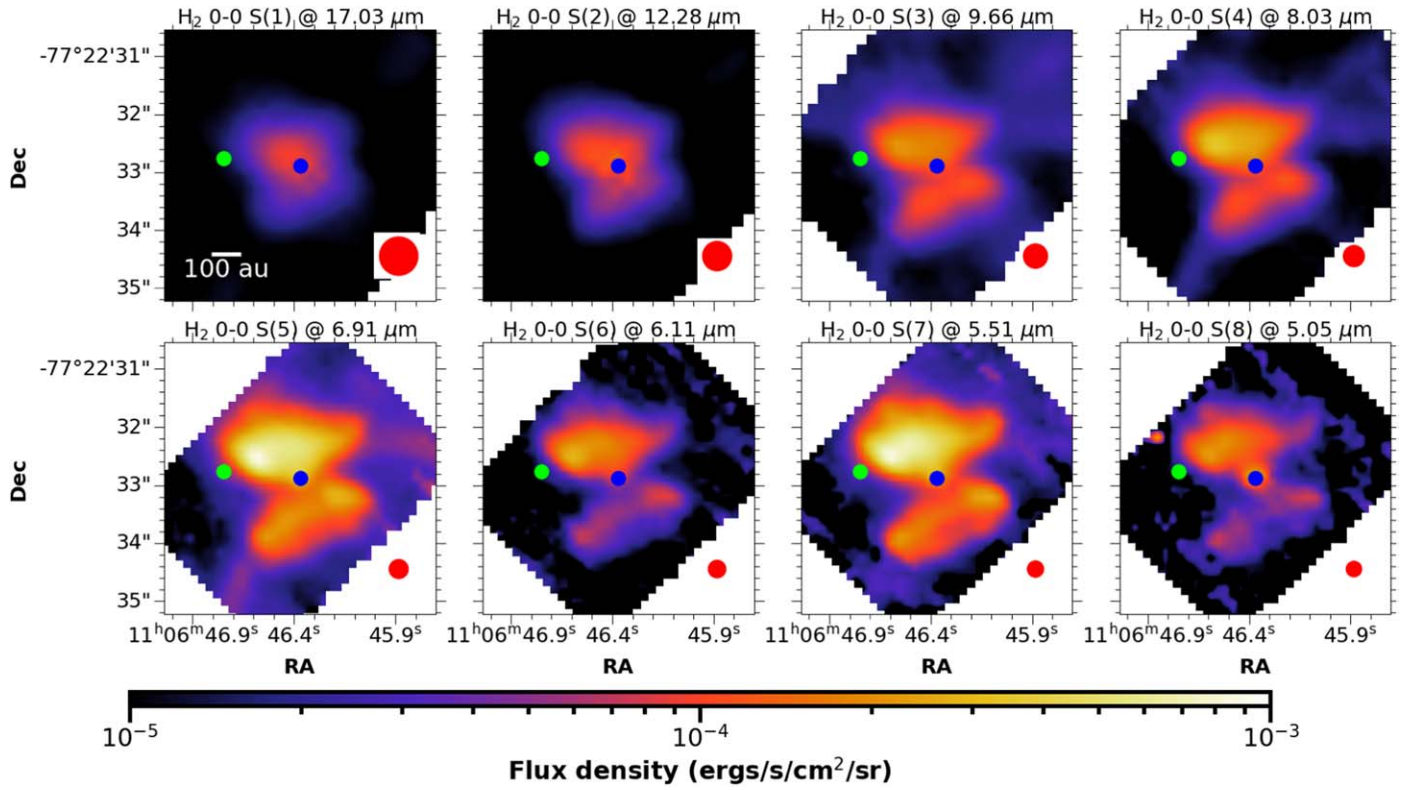

Figure 12. The morphology of the H_2 0–0 S line from S(1) to S(8) covering the MIRI MRS. All images are cropped to the same spatial scale of $5\farcs7 \times 5\farcs7$ and have the same color scale. The ALMA 1.3 mm position for Ced 110 IRS4A is shown as a blue circle, and that for IRS4B is shown as a lime circle. The scale bar corresponding to 100 au is shown in the lower left corner. The MIRI FWHM based on D. D. Law et al. (2023) is shown in the lower right corner as a red circle.

4. Discussion

4.1. Jet from Ced 110 IRS4A

The jet from Ced 110 IRS4A is detected in multiple transitions of [Fe II], as well as the [Ne II] line. While the jet is not completely captured in the FOV of the [Fe II] line at 5.34 μm (in MIRI channel-1 short FOV $\sim 3\farcs2 \times 3\farcs2$), the [Fe II] line at 26 μm in MIRI channel-4 (with its much larger FOV of $7\farcs7 \times 7\farcs7$) has a spatial extent of $6\farcs8$ or 1285 au (when measured from tip to tip). If we correct for the inclination of the protostar (76°), we find that the total jet length is 1324 au (assuming that the jet does not extend beyond the JWST footprint). From our PV analysis, we also know that the velocity of the jet is about 124 km s^{-1} (after correcting for inclination). Therefore, we can derive a dynamical timescale of the atomic jet (within the MIRI FOV) of ~25 yr.

Unlike the other atomic jets that have been detected with JWST from low-mass stars with a typical opening angle of $\leqslant 10°$ (M. Narang et al. 2024; S. Federman et al. 2025, in preparation), the atomic jet from Ced 110 IRS4A has a much larger opening angle Θ of $23° \pm 4°$. This suggests that the jet is not confined. If the jet were ballistically confined, then, given the jet velocity of 124 km s^{-1} and under the assumption that the shock temperature is 10,000 K (e.g., T. P. Ray & J. Ferreira 2021) with sound speed $c_s = 10$ km s^{-1}, the opening angle Θ would be $4\fdg6$, much smaller than what is measured. J. Sai et al. (2023) found that disks of Ced 110 IRS4A and IRS4B are misaligned with each other. This misalignment may result from dynamical interactions between the primary and secondary components, potentially leading to jet precession. Such precession might, in turn, produce a jet with a broader opening angle. This still does not explain the goblet-like structure seen in the [Fe II] line at 5.34 μm. One possible scenario to explain the wide-angle component is that in the past the launching mechanism for the [Fe II] was different from what it is today. Detailed discussion of the launching mechanism of the jet and outflow from the Ced 110 IRS4 system will be presented in a later work.

The jet from Ced 110 IRS4B seems to be more extended and brighter on the southern side, which is opposite to the jet from Ced 110 IRS4A. One possible explanation for this could be that the disk inclination of the IRS4B is opposite to that of IRS4A. This suggests that the disk inclination may be different for the two protostars.

4.2. Origin of Molecular Emission from Ced 110 IRS4A

Unlike the atomic and FS emission observed from Ced 110 IRS4, the molecular H_2 emission from the protostar is considerably broader and lacks any collimated components. Moreover, the distribution of H_2 emission around the protostar is notably asymmetric. The northern outflow region is not only brighter but also more extended compared to the southern region. This asymmetry indicates potential variations in the environmental conditions or the dynamics of the outflow in different directions, possibly influenced by the surrounding material. This north–south asymmetry could also be because of the geometrical effect, i.e., the northern side of the outflow is on the near side. This geometrical configuration is consistent with the brightness asymmetry shown in the gas disk in ^{12}CO (and probably ^{13}CO as well) and 1.3 mm dust continuum (J. Sai et al. 2023). This configuration is also consistent with the north–south asymmetry seen in FS lines.

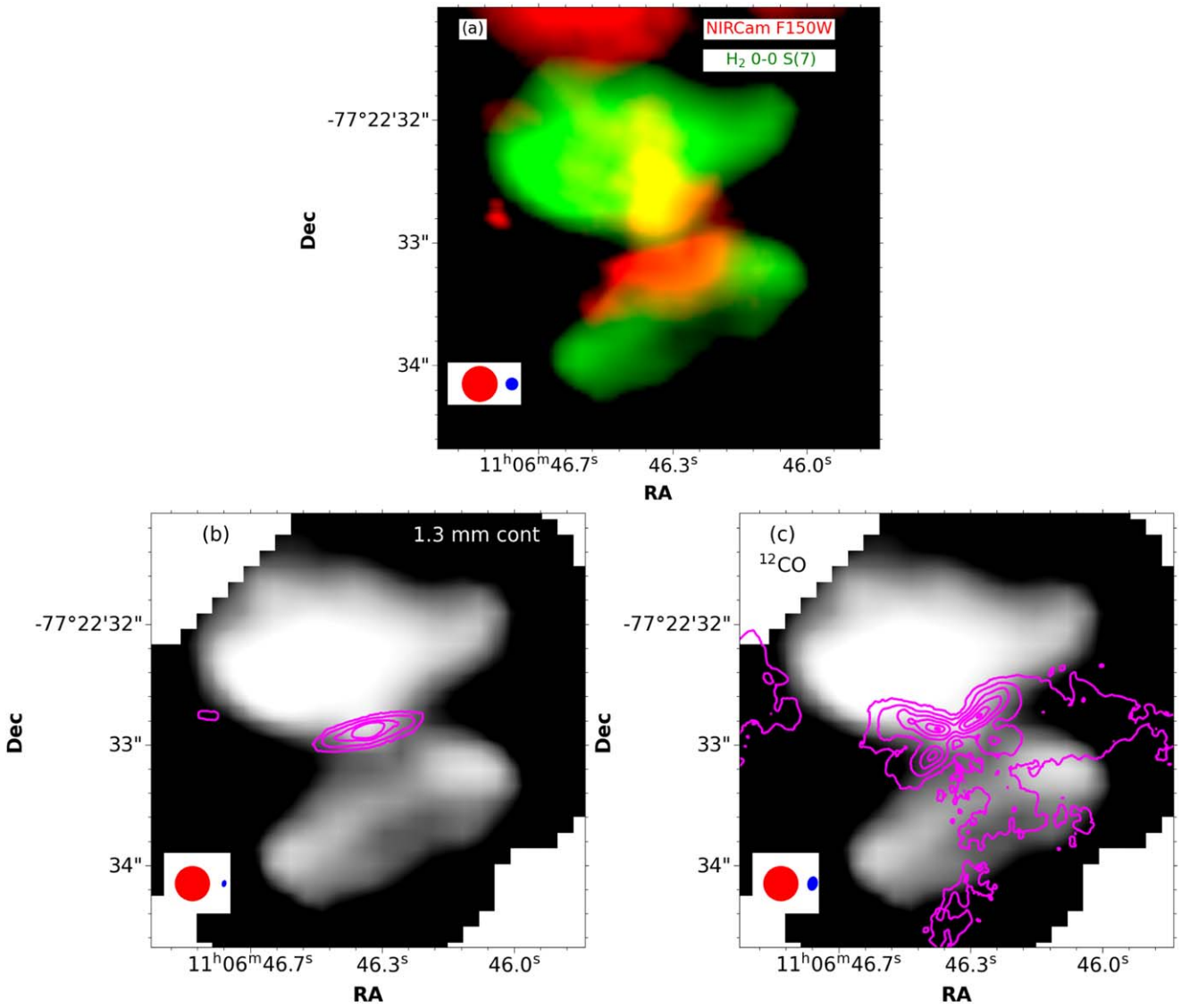

Figure 13. The molecular H_2 0–0 S(7) line with the NIRCam F150W emission, the SBLB 1.3 mm ALMA continuum, and the ALMA ^{12}CO observations. The MIRI FWHM based on D. D. Law et al. (2023) is shown in the lower left corner as a red circle, while the NIRCam/ALMA beam is shown as a blue ellipse.

In Figure 14, we provide a detailed comparison of the spatial extent of H_2 emission across three specific rotational transitions: 0–0 S(1), 0–0 S(4), and 0–0 S(7). These transitions represent different energy levels of the H_2 molecule. Our analysis reveals that the extent of the outflow is similar across these transitions, suggesting a consistent outflow structure across different excitation conditions of H_2. In Figure 14(a) we show the contours of H_2 0–0 S(4) and 0–0 S(7) overlaid on H_2 0–0 S(1), the lowest-lying transition of H_2 available in the JWST MIRI MRS. Interestingly, despite the higher spatial resolution of the H_2 0–0 S(7) transition compared to the H_2 0–0 S(1) transition, the overall extent of the emission remains similar.

To quantify this result, we measure the width of the H_2 emission across these transitions. To do so, we first need to detect the edge of the outflow. For this we make use of the Sobel–Feldman operator or Sobel filter (I. Sobel & G. Feldman 2015) using the implementation from the "*skimage*" Python package (S. van der Walt et al. 2014). The Sobel filter is a gradient-based edge detection technique. It computes the rate of change in intensity (gradient) in both the *x*- and *y*-directions and combines them to highlight edges. It works by convolving the image with two 3 × 3 kernels (one for horizontal changes and one for vertical changes) and computing the gradient. We start by rotating the image using the "scipy" Python package (P. Virtanen et al. 2020) to align the outflow axis along the *y*-direction by rotating the image by 14°. A similar approach is also followed in N. M. Habel et al. (2021) and I. Pascucci et al. (2024). We then applied the Sobel filter on the H_2 images to determine the edges of the outflow.

In Figure 14(b) we show the implementation of the Sobel filter and the edge detection for the H_2 0–0 S(4) transition. As can been seen from the figure, we are able to detect the edge of the H_2 emission. We next measured the width of the outflow. Figure 14(c) shows that the width of the outflow is similar across the three transitions (0–0 S(1), S(4), and S(7)) despite the varying angular resolution. This is counter to what has previously been detected in other protostars. It is found that higher-*J* transitions of H_2 tend to be more collimated than the lower-*J* transitions (e.g., M. Narang et al. 2025, in preparation; I. Pascucci et al. 2024; Ł. Tychoniec et al. 2024). This has been argued as evidence for disk winds as the outflow launching

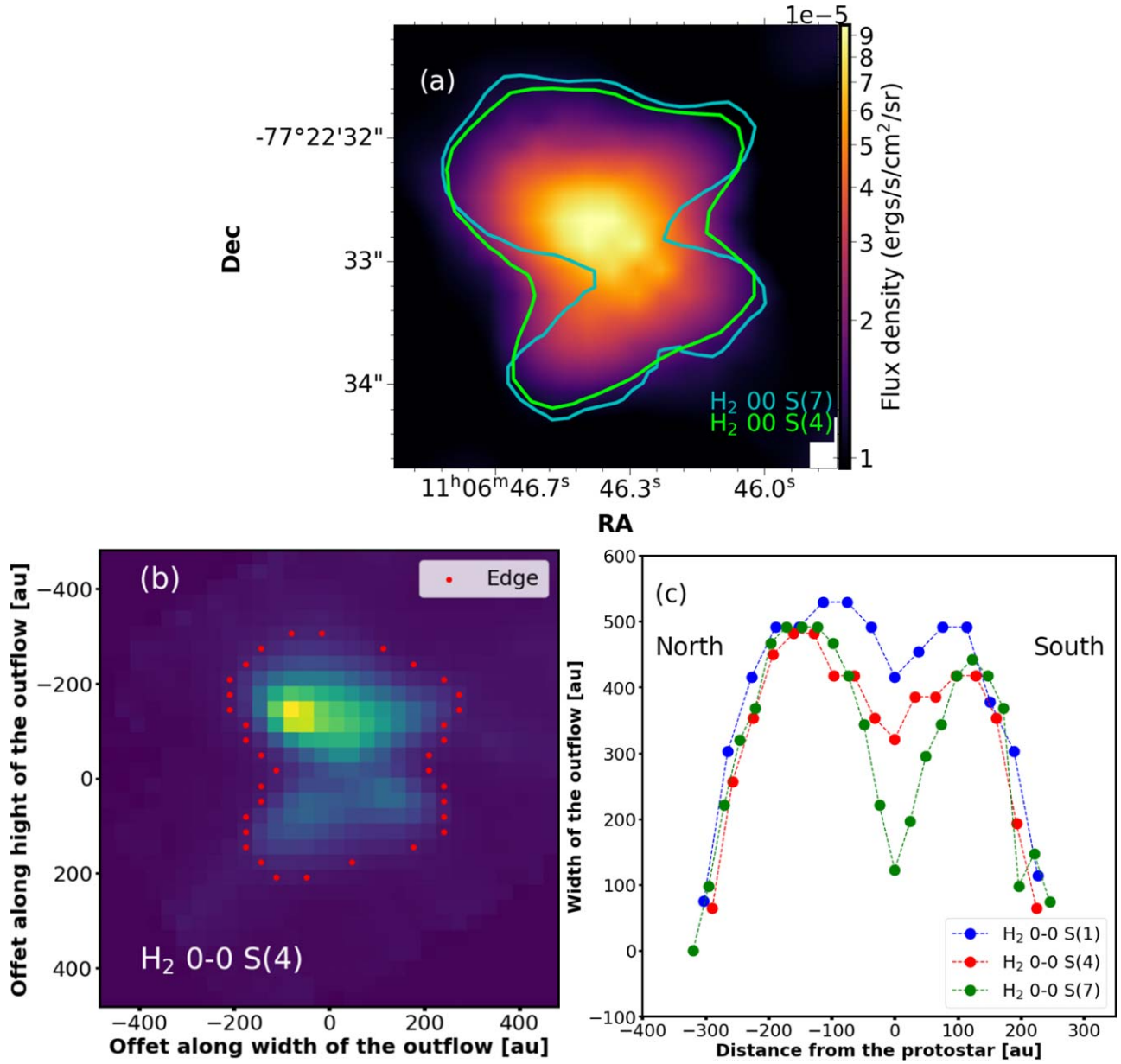

Figure 14. (a) The molecular H_2 0–0 S(1) line, with contours of 0–0 S(4) and 0–0 S(7) overlaid on top. The H_2 0–0 S(4) and H_2 0–0 S(7) contours are at 10% of the peak flux density (3.55×10^{-4} erg s^{-1} cm^{-2} sr^{-1} and 8.5×10^{-4} erg s^{-1} cm^{-2} sr^{-1}, respectively) of the emission. (b) The edge detected (in red) on top of the H_2 0–0 S(4) in color scale. (c) The outflow width as a function of distance from the protostar for the three (H_2 0–0 S(1), S(4), and (7)) transitions.

mechanism. Thus, this may suggest that MHD disk winds may not be the outflow launching mechanism. However, detailed modeling of the system and its outflow are necessary to completely rule this out.

Using a fit to the outflow width as measured with the H_2 0–0 S(7) transition, we can derive an upper limit to the width at the protostar. We find that the width of the outflow at the protostar is 130 ± 10 au. This is smaller than the disk diameter of 183.4 ± 0.4 au, as reported by J. Sai et al. (2023), but much larger than the upper limit of the width, 51 ± 8.6 au, that is derived for the [Fe II] jet.

5. Summary

In this work, we made use of NIRCam and MIRI observations from the Early Release Science Program IceAge, along with millimeter continuum and gas line data from the ALMA large program eDisk, to study the jet and outflow morphology from the Class 0/I protostar Ced 110 IRS4A and its companion Ced 110 IRS4B. The main results from these observations can be summarized as follows:

1. We detect Ced 110 IRS4A and Ced 110 IRS4B (a 0.02–0.05 $M_\odot$ substellar companion) with the NIRCam F150W and F410M observations. We also detect the disk shadow from both protostars in the F150W filter.
2. Both NIRCam scattered light and ALMA observations in continuum molecular lines exhibit arc-like structures associated with the Ced 110 IRS4 system.
3. MIRI MRS observations have detected a jet from the Class 0 protostar Ced 110 IRS4A in multiple [Fe II] lines, along with [Ni II] at 6.64 μm, [Ar II] at 6.99 μm, and

[Ne II] at 12.81 μm. This marks the first time a well-resolved jet has been detected from this system.
4. We also detect hints of [Fe II] and [Ni II] at 6.64 μm, [Ar II] at 6.99 μm, and [Ne II] at 12.81 μm originating from Ced 110 IRS4B. This could indicate a jet from a Ced 110 IRS4B as well.
5. The jet is quite wide, with the [Fe II] jet at 5.34 μm having an upper limit of the width at the base of 51 ± 8.6 au. This is much less than the disk diameter of 183.4 ± 0.4 au. The jet also has a large opening angle of $23^\circ \pm 4^\circ$, indicating a lack of collimation/confinement.
6. We find that the northern jet displays a blueshifted velocity while the southern side is redshifted. The jet has a velocity of 124 km s^{-1}, once corrected for inclination (inclination angle = 76°; J. Sai et al. 2023).
7. The molecular H_2 outflow displays a distinct morphology resembling two bowls or hemispheres placed back-to-back. The emission has a minimum at the location of the protostellar disk as detected with ALMA at 1.3 mm.
8. The extent of molecular H_2 emission is similar across the different transitions, very different from what has previously been observed. This suggests that MHD disk winds may not be the launching mechanism for the outflow detected in H_2.
9. We find that the upper limit to the width of the outflow at the protostellar location is 130 ± 10 au, which is smaller than the disk diameter of 183.4 ± 0.4 au but much larger than the upper limit of the width, 51 ± 8.6 au, that is derived for the [Fe II] jet.

This work highlights the power of JWST and ALMA observations in understanding the jet and outflow processes from protostars. However, further modeling of the jet and outflow is necessary to understand the wide morphology of the emission and will be taken up in a future study.

Acknowledgments

This work is based on observations made with the NASA/ESA/CSA James Webb Space Telescope. The data were obtained from the Mikulski Archive for Space Telescopes at the Space Telescope Science Institute, which is operated by the Association of Universities for Research in Astronomy, Inc., under NASA contract NAS 5-03127 for JWST. This paper makes use of the following ALMA data: ADS/ JAO. ALMA#2019.1.00261.L; 2019.A.00034.S. ALMA is a partnership of ESO (representing its member states), NSF (USA), and NINS (Japan), together with NRC (Canada), MOST and ASIAA (Taiwan), and KASI (Republic of Korea), in cooperation with the Republic of Chile. The Joint ALMA Observatory is operated by ESO, AUI/NRAO, and NAOJ. The National Radio Astronomy Observatory is a facility of the National Science Foundation operated under cooperative agreement by Associated Universities, Inc. N.O. and M.N. acknowledge support from the National Science and Technology Council (NSTC) in Taiwan (NSTC 113-2112-M-001-037). M.N. would also like to acknowledge the support of Manoj P. and Himanshu Tyagi at the Tata Institute of Fundamental Research, along with the Investigating Protostellar Accretion IPA team for the detailed discussion on analysis of JWST data and reduction.

Facilities: JWST, ALMA.

Data Availability

All of the JWST data presented in this article were obtained from the Mikulski Archive for Space Telescopes (MAST) at the Space Telescope Science Institute. The specific observations analyzed can be accessed via DOI: 10.17909/9s60-p048. The ALMA observations were obtained as part of the ALMA large program Early Planet Formation in Embedded Disks eDisk (2019.1.00261.L, 2019.A.00034.S).

Appendix

Tables 1 and 2 show the final parameters of the ALMA maps that have been used in this analysis.

Table 3 shows the atomic and FS lines analyzed in this work from Ced 110 IRS4.

Table 4 shows the molecular H_2 lines detected in the outflow from Ced 110 IRS4.

Table 1
Parameters of the ALMA Maps Used

Name	Robust	Beam Size (PA)
	Short-baseline + Long-baseline (SBLB)	
1.3 mm continuum	0	$0\farcs054 \times 0\farcs035$ ($-12\fdg5$)
1.3 mm continuum	2	$0\farcs122 \times 0\farcs086$ ($-18\fdg9$)
^{12}CO $J = 2$–1	0.5	$0\farcs115 \times 0\farcs083$ ($-12\fdg5$)
^{13}CO $J = 2$–1	1	$0\farcs155 \times 0\farcs107$ ($-22\fdg2$)
C^{18}O $J = 2$–1	1	$0\farcs153 \times 0\farcs107$ ($-19\fdg4$)
	Short-baseline (SB)	
^{12}CO $J = 2$–1	0.5	$0\farcs465 \times 0\farcs261$ (13°)
^{13}CO $J = 2$–1	0.5	$0\farcs155 \times 0\farcs107$ ($22\fdg2$)
C^{18}O $J = 2$–1	0.5	$0\farcs153 \times 0\farcs107$ ($19\fdg4$)

Table 2
Characteristics of the NIRCam Filters Based on J. Rigby et al. (2023)

Name	Pivot λ (μm)	$\Delta\lambda$ (μm)	Empirical PSF FWHM (arcsec)
F140M	1.405	0.141	0.048
F150W	1.501	0.317	0.050
F410M	4.083	0.436	0.137

Note. Also see JWST NIRCam documentation https://jwst-docs.stsci.edu/jwst-near-infrared-camera/nircam-instrumentation/nircam-filters.

Table 3
The Ionic and Atomic Lines Reported in This Work

Wavelength (μm)	Species and Transition Upper State–Lower State		A_{ul} (s^{-1})	E_{up} (K)	FWHM (arcsec)	Line Flux IRS4A (erg $\times 10^{-15}$ s^{-1} cm^{-2})	Line Flux IRS4B ($\times 10^{-15}$ erg s^{-1} cm^{-2})	References
5.340	[Fe II]	$^4F_{9/2}$–$^6D_{9/2}$	2.37×10^{-5}	2694	0.282	1.17 ± 0.03	0.07 ± 0.01	(1, 2)
6.636	[Ni II]	$^2D_{3/2}$–$^2D_{5/2}$	5.54×10^{-2}	2168	0.325	7.4 ± 0.1	0.1 ± 0.005	(2)
6.985	[Ar II]	$^2P_{1/2}$–$^2P_{3/2}$	5.3×10^{-2}	2059	0.336	2.21 ± 0.02	0.16 ± 0.005	(2)
12.814	[Ne II]	$^2P_{1/2}$–$^2P_{3/2}$	8.32×10^{-3}	1123	0.53	7.97 ± 0.03	0.72 ± 0.01	(2)
17.936	[Fe II]	$^4F_{7/2}$–$^4F_{9/2}$	5.84×10^{-3}	3496	0.7	6.88 ± 0.07	0.8 ± 0.01	(2)
24.519	[Fe II]	$^4F_{5/2}$–$^4F_{7/2}$	3.93×10^{-3}	4083	0.915	3.42 ± 0.13	0.81 ± 0.14	(2)
25.249	[S I]	$^3P_1$–$^3P_2$	1.4×10^{-3}	570	0.94	12.0 ± 0.56	3.4 ± 0.2	(2)
25.988	[Fe II]	$^6D_{7/2}$–$^6D_{9/2}$	2.14×10^{-3}	554	0.963	25.4 ± 1.2	6.5 ± 0.4	(1, 2)

Note. The FWHM of the lines based on the empirical relationship from D. D. Law et al. (2023) is also provided.
References. (1) S. S. Tayal & O. Zatsarinny 2018; (2) A. Kramida et al. 2023.

Table 4
The H_2 Lines Analyzed in This Work

Wavelength (μm)	Name	A_{ul} (s^{-1})	E_{up} (K)	FHWM (arcsec)
5.053	H_2 0–0 S(8)	3.2×10^{-7}	8677	0.272
5.511	H_2 0–0 S(7)	2.0×10^{-7}	7196	0.288
6.109	H_2 0–0 S(6)	1.1×10^{-7}	5830	0.307
6.910	H_2 0–0 S(5)	5.9×10^{-8}	4586	0.334
8.025	H_2 0–0 S(4)	2.6×10^{-8}	3474	0.37
9.665	H_2 0–0 S(3)	9.8×10^{-9}	2503	0.425
12.279	H_2 0–0 S(2)	2.8×10^{-9}	1681	0.511
17.035	H_2 0–0 S(1)	4.8×10^{-10}	1015	0.668

Note. The wavelength, Einstein A-coefficient A_{ul}, and upper-state energy are from I. E. Gordon et al. (2022). The FWHM of the lines based on the empirical relationship from D. D. Law et al. (2023) is also provided.

ORCID iDs

Mayank Narang https://orcid.org/0000-0002-0554-1151
Nagayoshi Ohashi https://orcid.org/0000-0003-0998-5064
John J. Tobin https://orcid.org/0000-0002-6195-0152
M. K. McClure https://orcid.org/0000-0003-1878-327X
Jes K. Jørgensen https://orcid.org/0000-0001-9133-8047
Jinshi Sai (Insa Choi) https://orcid.org/0000-0003-4361-5577

References

Andre, P., Ward-Thompson, D., & Barsony, M. 1993, ApJ, 406, 122
Appel, S. M., Burkhart, B., Semenov, V. A., et al. 2023, ApJ, 954, 93
Assani, K., Harsono, D., Ramsey, J., et al. 2024, A&A, 688, A26
Bally, J. 2016, ARA&A, 54, 491
Beuther, H., van Dishoeck, E. F., Tychoniec, L., et al. 2023, A&A, 673, A121
Bourke, T. L., Crapsi, A., Myers, P. C., et al. 2005, ApJL, 633, L129
Brunken, N. G. C., Rocha, W. R. M., van Dishoeck, E. F., et al. 2024, A&A, 685, A27
Caratti o Garatti, A., Ray, T. P., Kavanagh, P. J., et al. 2024, A&A, 691, A134
Cassen, P., & Moosman, A. 1981, Icar, 48, 353
Di Francesco, J., Johnstone, D., Kirk, H., et al. 2008, ApJS, 175, 277
Dunham, M. M., Stutz, A. M., Allen, L. E., et al. 2014, Protostars and Planets VI, Vol. 195 (Tucson, AZ: Univ. Arizona Press)
Dutta, S., Lee, C.-F., Johnstone, D., et al. 2023, arXiv:2306.15346
Evans, N. J., Dunham, M. M., Jørgensen, J. K., et al. 2009, ApJS, 181, 321
Fall, S. M., Krumholz, M. R., & Matzner, C. D. 2010, ApJL, 710, L142
Federman, S. A., Megeath, S. T., Rubinstein, A. E., et al. 2024, ApJ, 966, 41
Federrath, C. 2015, MNRAS, 450, 4035
Fiorellino, E., Tychoniec, Ł., Cruz-Sáenz de Miera, F., et al. 2023, ApJ, 944, 135
Fiorellino, E., Tychoniec, Ł., Manara, C. F., et al. 2022, ApJL, 937, L9
Frank, A., Ray, T. P., Cabrit, S., et al. 2014, Protostars and Planets VI, Vol. 451 (Tucson, AZ: Univ. Arizona Press)
Gordon, I. E., Rothman, L. S., Hargreaves, R. J., et al. 2022, JQSRT, 277, 107949
Green, J. D., Pontoppidan, K. M., Reiter, M., et al. 2024, ApJ, 972, 5
Guszejnov, D., Grudić, M. Y., Offner, S. S. R., et al. 2022, MNRAS, 515, 4929
Habel, N. M., Megeath, S. T., Booker, J. J., et al. 2021, ApJ, 911, 153
Harsono, D., Bjerkeli, P., Ramsey, J. P., et al. 2023, ApJL, 951, L32
Hartmann, L., Herczeg, G., & Calvet, N. 2016, ARA&A, 54, 135
Hiramatsu, M., Hayakawa, T., Tatematsu, K., et al. 2007, ApJ, 664, 964
Huff, L. W. 2005, Proc. SPIE, 5904, 30
Jørgensen, J. K., Bourke, T. L., Myers, P. C., et al. 2007, ApJ, 659, 479
Jørgensen, J. K., van Dishoeck, E. F., Visser, R., et al. 2009, A&A, 507, 861
Koo, B.-C., Raymond, J. C., & Kim, H.-J. 2016, JKAS, 49, 109
Kramida, A., Ralchenko, Y., Reader, J. & NIST ASD Team 2023, NIST Atomic Spectra Database, v5.11, National Institute of Standards and Technology, https://physics.nist.gov/asd
Lahuis, F., van Dishoeck, E. F., Jørgensen, J. K., et al. 2010, A&A, 519, A3
Law, D. D., Morrison, J. E., Argyriou, I., et al. 2023, AJ, 166, 45
Lebreuilly, U., Hennebelle, P., Maury, A., et al. 2024, A&A, 683, A13
Lee, C.-F. 2020, A&ARv, 28, 1
Lee, C.-F., Ho, P. T. P., Li, Z.-Y., et al. 2017, NatAs, 1, 0152
Lee, C.-F., Tabone, B., Cabrit, S., et al. 2021, ApJL, 907, L41
Manoj, P., Kim, K. H., Furlan, E., et al. 2011, ApJS, 193, 11
Matsushita, Y., Takahashi, S., Machida, M. N., et al. 2019, ApJ, 871, 221
McClure, M. K., Rocha, W. R. M., Pontoppidan, K. M., et al. 2023, NatAs, 7, 431
McMullin, J. P., Waters, B., Schiebel, D., et al. 2007, adass XVI, 376, 127
Narang, M., Manoj, P., Tyagi, H., et al. 2023, JApA, 44, 92
Narang, M., Manoj, P., Tyagi, H., et al. 2024, ApJL, 962, L16
Nazari, P., Rocha, W. R. M., Rubinstein, A. E., et al. 2024, A&A, 686, A71
Neufeld, D. A., Manoj, P., Tyagi, H., et al. 2024, ApJL, 966, L22
Nisini, B., Navarro, M. G., Giannini, T., et al. 2024, ApJ, 967, 168
Offner, S. S. R., & Arce, H. G. 2014, ApJ, 784, 61
Ohashi, N., Tobin, J. J., Jørgensen, J. K., et al. 2023, ApJ, 951, 8
Pascucci, I., Beck, T. L., Cabrit, S., et al. 2024, NatAs, 9, 81
Persi, P., Marenzi, A. R., Gómez, M., et al. 2001, A&A, 376, 907
Pinte, C., Ménard, F., Duchêne, G., et al. 2018, A&A, 609, A47
Podio, L., Tabone, B., Codella, C., et al. 2021, A&A, 648, A45
Pokhrel, R., Megeath, S. T., Gutermuth, R. A., et al. 2023a, ApJS, 266, 32
Pokhrel, R., Megeath, S. T., Gutermuth, R. A., et al. 2023b, Extension of HOPS Out to 500 ParSecs, IPAC, doi:10.26131/IRSA553
Pontoppidan, K. M., & Dullemond, C. P. 2005, A&A, 435, 595
Prusti, T., Clark, F. O., Whittet, D. C. B., et al. 1991, MNRAS, 251, 303
Pudritz, R. E., Ouyed, R., Fendt, C., et al. 2007, Protostars and Planets V (Tucson, AZ: Univ. Arizona Press), 277
Ray, T. P., & Ferreira, J. 2021, NewAR, 93, 101615
Ray, T. P., McCaughrean, M. J., Caratti o Garatti, A., et al. 2023, Natur, 622, 48
Reipurth, B., Heathcote, S., Morse, J., et al. 2002, AJ, 123, 362
Reiter, M., & Smith, N. 2013, MNRAS, 433, 2226
Rieke, G. H., Wright, G. S., Böker, T., et al. 2015, PASP, 127, 584
Rigby, J., Perrin, M., McElwain, M., et al. 2023, PASP, 135, 048001
Rocha, W. R. M., McClure, M. K., Sturm, J. A., et al. 2025, A&A, 693, A288
Rosenfeld, K. A., Andrews, S. M., Hughes, A. M., et al. 2013, ApJ, 774, 16
Rubinstein, A. E., Tyagi, H., Nazari, P., et al. 2024, ApJ, 974, 112
Sai, J., Yen, H.-W., Ohashi, N., et al. 2023, ApJ, 954, 67
Shang, H., Li, Z.-Y., & Hirano, N. 2007, Protostars and Planets V (Tucson, AZ: Univ. Arizona Press), 261
Slavicinska, K., van Dishoeck, E. F., Tychoniec, Ł., et al. 2024, A&A, 688, A29
Sobel, I., & Feldman, G. 2015, An Isotropic 3 × 3 Image Gradient Operator, doi:10.13140/RG.2.1.1912.4965
Tayal, S. S., & Zatsarinny, O. 2018, PhRvA, 98, 012706
Tobin, J. J., & Sheehan, P. D. 2024, ARA&A, 62, 203
Tyagi, H., Manoj, P., Narang, M., et al. 2024, arXiv:2410.06697
Tychoniec, Ł., van Gelder, M. L., van Dishoeck, E. F., et al. 2024, A&A, 687, A36
Ulrich, R. K. 1976, ApJ, 210, 377
van der Walt, S., Schönberger, J. L., Nunez-Iglesias, J., et al. 2014, PeerJ, 2, e453
van Kempen, T. A., van Dishoeck, E. F., Hogerheijde, M. R., et al. 2009, A&A, 508, 259
Virtanen, P., Gommers, R., Oliphant, T. E., et al. 2020, NatMe, 17, 261
Watson, D. M., Calvet, N. P., Fischer, W. J., et al. 2016, ApJ, 828, 52
White, R. J., Greene, T. P., Doppmann, G. W., et al. 2007, Protostars and Planets V (Tucson, AZ: Univ. Arizona Press), 117
White, R. J., & Hillenbrand, L. A. 2004, ApJ, 616, 998
Wright, G. S., Wright, D., Goodson, G. B., et al. 2015, PASP, 127, 595
Yang, Y.-L., Green, J. D., Pontoppidan, K. M., et al. 2022, ApJL, 941, L13
Zinnecker, H., Krabbe, A., McCaughrean, M. J., et al. 1999, A&A, 352, L73